ChemPubSoc Europe

DOI: 10.1002/chem.201302455

CHEMISTRY
A European Journal
Full Paper

MOFs

Modification of Extended Open Frameworks with Fluorescent Tags for Sensing Explosives: Competition between Size Selectivity and Electron Deficiency

Bappaditya Gole, Arun Kumar Bar, and Partha Sarathi Mukherjee*[a]

Abstract: Three new electron-rich metal–organic frameworks (**MOF-1**–**MOF-3**) have been synthesized by employing ligands bearing aromatic tags. The key role of the chosen aromatic tags is to enhance the π-electron density of the luminescent MOFs. Single-crystal X-ray structures have revealed that these MOFs form three-dimensional porous networks with the aromatic tags projecting inwardly into the pores. These highly luminescent electron-rich MOFs have been successfully utilized for the detection of explosive nitroaromatic compounds (NACs) on the basis of fluorescence quenching. Although all of the prepared MOFs can serve as sensors for NACs, **MOF-1** and **MOF-2** exhibit superior sensitivity towards 4-nitrotoluene (4-NT) and 2,4-dinitrotoluene (DNT) compared to 2,4,6-trinitrotoluene (TNT) and 1,3,5-trinitrobenzene (TNB). **MOF-3**, on the other hand, shows an order of sensitivity in accordance with the electron deficiencies of the substrates. To understand such anomalous behavior, we have thoroughly analyzed both the steady-state and time-resolved fluorescence quenching associated with these interactions. Determination of static Stern–Volmer constants (K_S) as well as collisional constants (K_C) has revealed that **MOF-1** and **MOF-2** have higher K_S values with 4-NT than with TNT, whereas for **MOF-3** the reverse order is observed. This apparently anomalous phenomenon was well corroborated by theoretical calculations. Moreover, recyclability and sensitivity studies have revealed that these MOFs can be reused several times and that their sensitivities towards TNT solution are at the parts per billion (ppb) level.

Introduction

An increasing number of terror attacks using explosive chemicals in several countries have become recent threats to our daily life. Although various diverse explosives are commercially available, a large number of them include nitro- or nitroaromatic compounds.[1] The most commonly used explosive ingredients are 2,4,6-trinitrotoluene (TNT), 1,3,5-trinitrobenzene (TNB), 1,3-dinitrobenzene (DNB), 2,4-dinitrotoluene (DNT), and so on.[2] Moreover, NACs are the main constituents of many unexploded landmines used worldwide during World War II, and even today these NACs remain as important energetic materials for the preparation of landmines.[3] Notably, NACs are also widely used in the agrochemical industry.[4] There are many environmental and safety concerns relating to the use of NACs.[5] It has been found that exposure to TNT can lead to anaemia and abnormal liver function.[6] Due to its adverse health effects, the US Environmental Protection Agency (EPA) has stipulated a maximum permissible level of TNT in drinking water of around 2 ppb.[7] Therefore, the sensing of NACs is a growing concern for both security reasons and pollution control.[8]

Although various techniques are known for the detection of explosives,[9] many of them are expensive, less sensitive, and not suitable for in-field application.[10] Metal detectors are commonly used to detect explosives, but by definition are limited to the detection of metal-based weapons. Canines are also used for this purpose, being among the most reliable and effective detectors at our disposal.[3] Fluorescence-based chemosensors offer several advantages over other approaches because of their high sensitivity, and can be used in hand-held devices for in-field detection. A wide variety of luminescence-based sensors for NACs are known in the literature,[11] such as metal complexes,[12,13] supramolecular polymers,[14] carbon nanotubes,[15] conjugated polymers,[16] and dendrimers,[17] as well as metal–organic frameworks as a new generation of sensors for the sensing of explosives.[18] In the majority of cases, the sensing event mainly relies on an oxidative quenching mechanism. Generally, sensors act as electron donors and, due to the presence of their electron-withdrawing nitro group(s), NACs act as electron acceptors. Upon photo-excitation, a sensor molecule transfers an electron to the analyte, leading to oxidation of the excited state, which in turn quenches the fluorescence. Conjugated polymers have been well studied and have been shown to be very efficient sensors because of their higher ability to donate electrons, which is further enhanced by their delocalized π* excited states.[16] Moreover, a conjugated polymeric backbone facilitates exciton migration

---

[a] *B. Gole, Dr. A. K. Bar, Prof. P. S. Mukherjee*
Department of Inorganic and Physical Chemistry
Indian Institute of Science
Bangalore-560012 (India)
Fax: (+91) 80-2360-1552
E-mail: psm@ipc.iisc.ernet.in

Supporting information for this article is available on the WWW under http://dx.doi.org/10.1002/chem.201302455.

upon excitation to enhance their sensitivity. However, real-time application of these materials is still limited due to various issues. Firstly, the traditional synthesis of these covalent organic polymers involves a multi-step process and in many cases it ends in a low yield of the target product. Secondly, control over the molecular organization or determination of structure is not an easy task, mainly because of their non-crystalline nature and/or poor solubility.

In recent times, metal–organic frameworks have attracted enormous attention because of their high surface areas, high thermal stability, and the tunability of their porous structures.[19] To date, they have been widely used for gas storage,[20] gas separation,[21] drug delivery,[22] imaging,[23] and heterogeneous catalysis.[24,25] Luminescent metal–organic frameworks can also be used for chemosensing.[26] The well-defined pore structure and the ordered nature of these frameworks facilitate rapid and selective detection of NACs. The selectivity and sensitivity mainly depend on the electron density and the ability of the MOFs to donate electrons. Recently, a few luminescent MOFs have been reported for the sensing of explosives based on the concept of introducing electron-rich π-conjugated fluorescent ligands,[18] which mainly gives rise to luminescence in the backbone of the MOFs.

Herein, we report a new strategy of using polyaromatic moieties as fluorescent tags for systematic tuning of the sensitivity and selectivity of MOFs. Although the concept of using fluorescent tags for tuning selectivity and sensitivity is quite common in bio-sensing applications, our present approach of using aromatic tags to tune the efficiency of MOFs for sensing explosives is new. The ligands 5-(benzyloxy)isophthalic acid (**H_2L^1**), 5-(naphthalen-1-ylmethoxy)isophthalic acid (**H_2L^2**), and 5-(pyren-1-ylmethoxy)isophthalic acid (**H_2L^3**), with increasing order of π-electron density in the aromatic tags (phenyl, naphthyl, and pyrenyl; Scheme 1) have been synthesized, characterized, and successfully employed in the synthesis of three new MOFs (**MOF-1**–**MOF-3**). The introduction of these tags was anticipated to enhance the selectivity and sensitivity for the detection of NACs. In addition, we have also focused on the mechanisms of the sensing of NACs, which should aid the future design of better sensors. The present study has also revealed a competition between size selectivity and electron deficiency of the NACs. The observed experimental phenomenon has been well corroborated by theoretical band structure calculations on the MOFs.

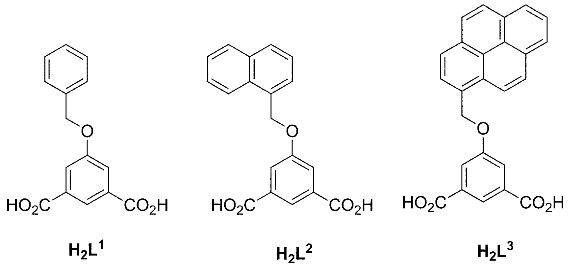

Scheme 1. Acids used in this study.

Results and Discussion

We have designed and synthesized three new ligands, **H_2L^1**, **H_2L^2**, and **H_2L^3**, with two distinct functionalities, namely isophthalic acid (*iph*) and a fluorophore. The *iph* unit was used to generate a coordination polymer backbone with metal ion connectors, and the fluorophores served as fluorescent tags to enhance the electron density in the MOFs for sensing electron-deficient species. Phenyl, naphthyl, and pyrenyl groups were used as tags to tune the π-electron densities of the resulting MOFs in increasing order. Additionally, 1,4-di(4-pyridyl)benzene (dpb) was employed as an interlinking unit to enhance the microporosity of the three-dimensional (3D) networks. Solvothermal reactions of the respective ligands in dimethyl formamide (DMF) with $Zn(NO_3)_2{\cdot}6H_2O$ at 120 °C for 24 h furnished 3D networks for each of the MOFs in excellent yields.

Single-crystal X-ray diffraction analyses (Table 1) showed the 3D networks of **MOF-1** and **MOF-3** to be isostructural (Figures 1 and 2), although they crystallized in different crystal systems (triclinic *P*1 for **MOF-1** and orthorhombic *Pba*2 for **MOF-3**). Moreover, they possessed similar 3D porous networks with moderately solvent-accessible 3D pores of 45% (for **MOF-1**) and 9.8% (for **MOF-3**) of the total volume, as calculated using PLATON. Though several attempts to obtain suitable single crystals of **MOF-2** were unsuccessful, the PXRD pattern indicated that the as-synthesized **MOF-2** was isostructural with **MOF-1** and **MOF-3** (Figure 3).

In the frameworks, the *iph* moieties of the ligands are involved in the formation of two-dimensional layered networks connecting distorted octahedral Zn^{2+} ions. The equatorial sites of each Zn^{2+} ion are coordinated to four O atoms of three different *iph* units with average bond distances of 2.165 Å (for

Table 1. Crystallographic parameters of **MOF-1** and **MOF-3**.

	MOF-1	**MOF-3**
Empirical formula	$C_{31}H_{22}N_2O_5Zn$	$C_{41}H_{26}N_2O_5Zn$
Fw	567.89	692.03
T [K]	90(2)	90(2)
Crystal system	triclinic	orthorhombic
Space group	*P*1	*Pba*2
a [Å]	15.657(2)	15.749(10)
b [Å]	15.672(2)	16.425(11)
c [Å]	16.339(2)	15.725(11)
α [deg]	89.9(2)	90.00
β [deg]	89.9(8)	90.00
γ [deg]	81.9(1)	90.00
V [Å^3]	3968.6(8)	4068(5)
Z	1	4
ρ_{calcd} [g cm^{-3}]	0.950	1.227
$\mu(Mo_{K\alpha})$ [mm^{-1}]	0.648	0.652
λ [Å]	0.71073	0.71073
F (000)	1167.0	1554.9
Collected reflns.	64323	14304
Unique reflns.	29368	7113
GOF (F^2)	1.129	0.971
R_1[a]	0.1251	0.1065
wR_2[b]	0.3198	0.2930

[a] $R_1 = \Sigma|F_o - F_c|/\Sigma|F_o|$; [b] $wR_2 = \Sigma[w(F_o^2 - F_c^2)^2]/w(F_o^2)^2]^{1/2}$.

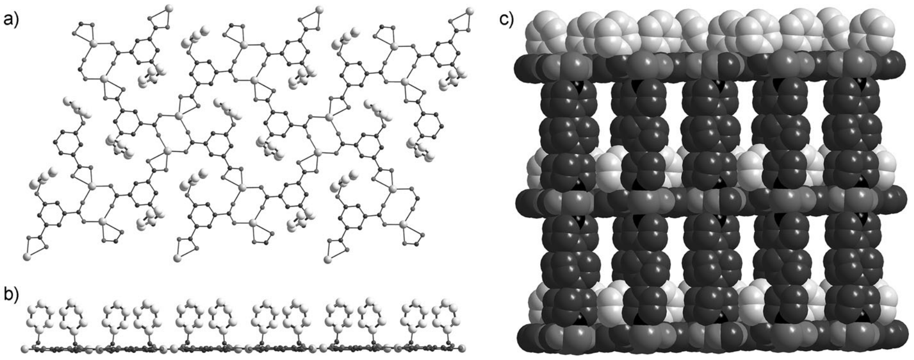

Figure 1. Crystal structure of **MOF-1**. (a) Two-dimensional layered network involving *iph* units of $\mathbf{H_2L^1}$ and Zn^{2+} ions. (b) The functionalized phenyl moieties residing above the layer. (c) Space-filling representation of **MOF-1**. The fluorescent tags are located inside the channels. The phenyl moieties are shown in a light-gray color.

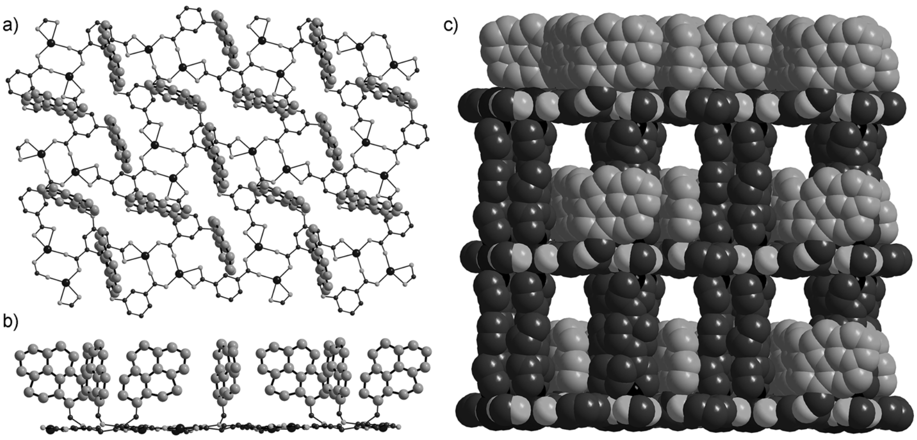

Figure 2. Crystal structure of **MOF-3**. (a) Two-dimensional layered network involving *iph* units of $\mathbf{H_2L^3}$ and Zn^{2+} ions. (b) Projection of functionalized pyrene moieties residing above the layer. (c) Space-filling representation of **MOF-3**. The pyrene tags are situated inside the channels. The pyrene moieties are shown in a light-gray color.

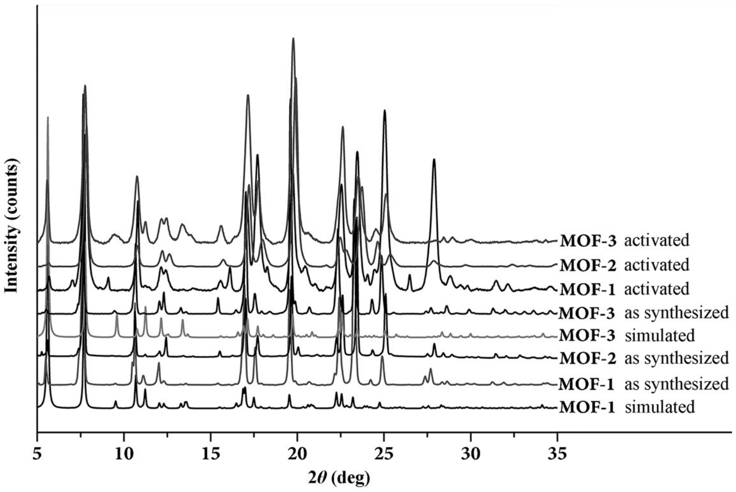

Figure 3. PXRD patterns of as-synthesized and activated **MOF-1**–**MOF-3**, and simulated PXRD patterns of **MOF-1** and **MOF-3**.

MOF-1) and 2.145 Å (for **MOF-3**). In both cases, the fluorophores reside below (or above) the 2D layered networks (Figure 1b and Figure 2b). These 2D layers are interconnected by 1,4-di(4-pyridyl)benzene units coordinated at the axial positions of the Zn^{2+} ions, giving rise to 3D MOFs with large porous channels. Interestingly, the phenyl or pyrenyl groups attached to the polymeric backbone of the frameworks occupied the pores and acted as fluorescent tags.

The phase purities and thermal stabilities of the MOFs were checked by PXRD and thermogravimetric analysis (TGA). Comparison of the simulated PXRD patterns of **MOF-1** and **MOF-3** with that of the as-synthesized **MOF-2** indicated that **MOF-2** adopted a similar molecular structure to those of **MOF-1** and **MOF-3** (Figure 3). The PXRD patterns of the activated samples (details of the procedure for activation of the MOFs are given in the Experimental Section) indicated stability of their networks even after removal of the solvent molecules from the pores. TGA revealed a consistent weight loss of about 20% for all three MOFs up to 200 °C, which is attributed to the removal of water and DMF. All of the MOFs showed similar thermal stability up to around 280 °C. The activated samples displayed similar thermal stabilities to those of the as-synthesized samples (Figure 4).

Photophysical properties

The ligands $\mathbf{H_2L^1}$, $\mathbf{H_2L^2}$, and $\mathbf{H_2L^3}$ showed their characteristic photoluminescence emission maxima at 335, 340, and 375 nm upon excitation at 306, 283, and 345 nm, respectively. The photoluminescence behaviors of $\mathbf{H_2L^2}$ and $\mathbf{H_2L^3}$ closely resembled those of naphthalene and pyrene, respectively. This confirmed that these fluorescent tags were the origin of the photoluminescence of these ligands. **MOF-1**–**MOF-3**, constructed from d^{10} (Zn^{2+}) ions, showed excellent photoluminescence (PL) properties, making them promising as photoactive materials. The PL spectra of dispersions of **MOF-1**–**MOF-3** in ethanol at room temperature (Supporting Information) showed strong emission bands at $\lambda_{em}=415$, 420, and 480 nm upon excitation at 310, 300, and 360 nm, respectively. The strong red-shifts of the emission maxima of the MOFs compared to

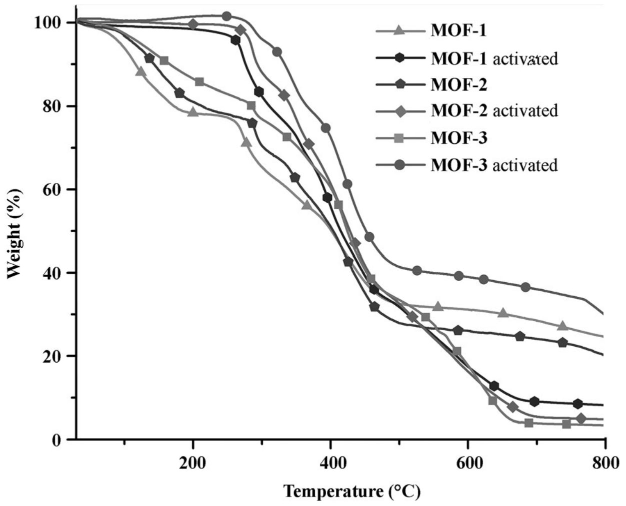

Figure 4. TGA plots of **MOF-1**–**MOF-3** along with their activated forms.

their parent ligands is most probably due to substantial electronic coupling between neighboring ligands through the Zn^{2+} ions.

Sensing of nitroaromatics

The chemical structures of the MOFs incorporated electron-rich fluorophores with increasing electron density: phenyl, naphthyl, and pyrenyl for **MOF-1**–**MOF-3**, respectively. To probe the applicability of these MOFs for the sensing of electron-deficient nitroaromatics (NACs), the PL properties of their dispersions in ethanol were investigated. The PL intensities of the MOFs were found to increase in the order **MOF-1** < **MOF-2** < **MOF-3** under similar experimental conditions (slit width 2 nm). This trend can be mainly ascribed to the incorporation of electron-rich fluorophores that essentially enhance the electron density in the MOFs. Addition of small amounts of different NACs to dispersions of **MOF-1**–**MOF-3** resulted in quenching of the photoluminescence intensities.

The NACs used in this study were 1,3,5-trinitrobenzene (TNB), 2,4,6-trinitrotoluene (TNT), 2,4-dinitrotoluene (2,4-DNT), 3,4-dinitrotoluene (3,4-DNT), 3,5-dinitrobenzoic acid (3,5-DNBA), 3-nitrobenzoic acid (3-NBA), 4-nitrobenzoic acid (4-NBA), 4-nitrotoluene (4-NT), and nitrobenzene (NB). A few simple electron-rich aromatic compounds (*p*-xylene, *p*-cresol, and 4-methoxybenzoic acid) were also examined. A few electron-deficient non-nitro-aromatic compounds, namely chlorobenzene, 1,2-dichlorobenzene, and benzoic acid, were also used to assess the selectivity of the sensing of nitroaromatics.

To gain a better understanding of the ability of these MOFs to sense NACs, PL quenching titrations were performed by gradual addition of 10 mm stock solutions of different analytes to the MOFs dispersed in ethanol. Changes in the PL intensities of all of the MOFs upon titration with TNT are shown in Figure 5, and the results with other NACs are provided in the Supporting Information.

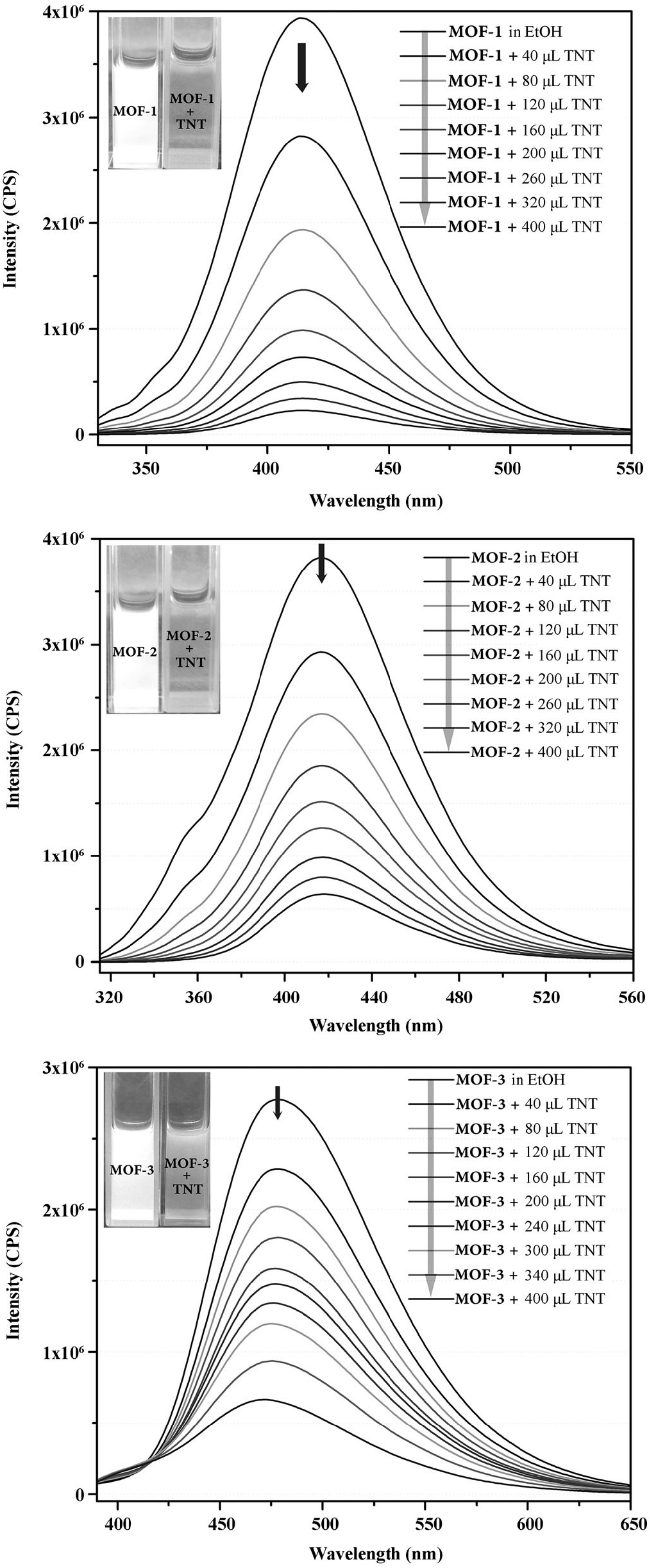

Figure 5. Reduction in the PL emission intensities of the MOFs upon gradual addition of TNT. Inset: MOFs before and after titration with TNT under UV light.

Interestingly, selectivity experiments on each of the MOFs revealed that all of the NACs showed significant quenching responses over the other non-nitro analytes (Figure 6). The inability of the non-nitro analytes to quench the fluorescence

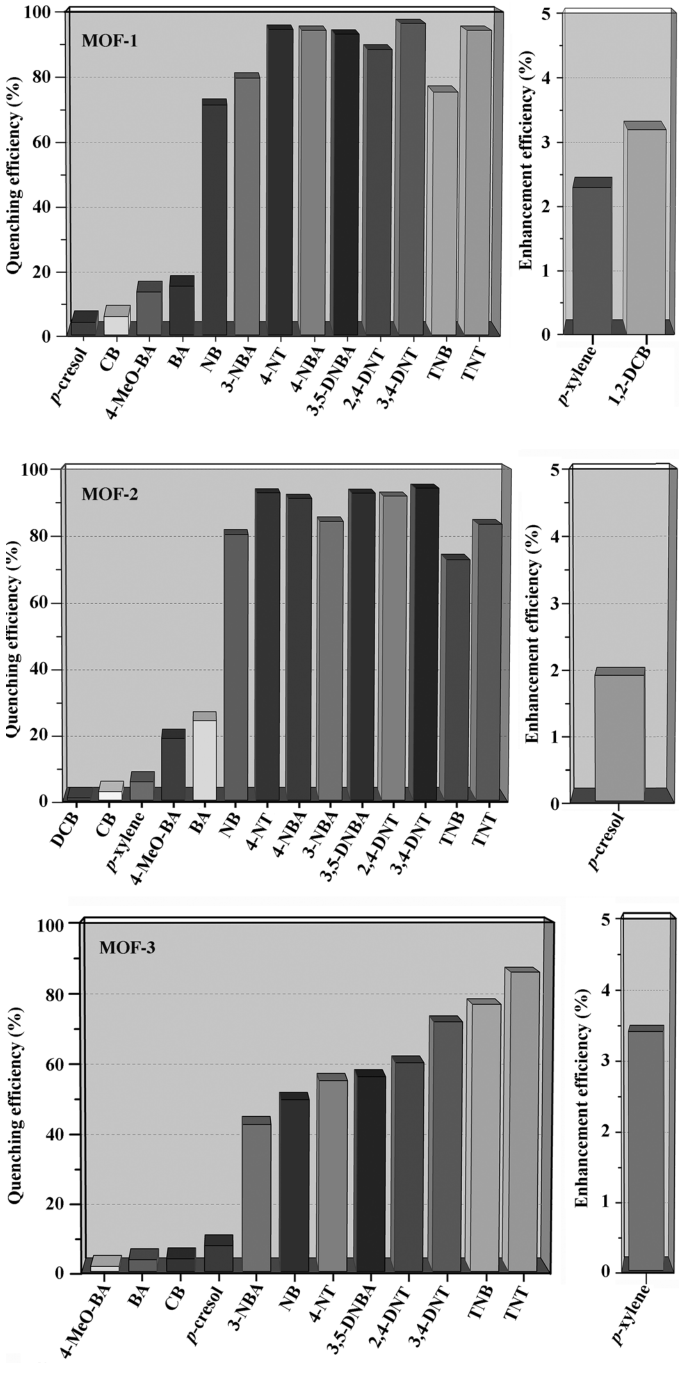

Figure 6. Reductions in fluorescence intensities (plotted as quenching efficiencies) observed upon addition of 400 μL of 10 mM stock solutions of several quenchers to dispersions of the MOFs in ethanol (left). Enhancements (plotted as an enhancement efficiency %) in fluorescence intensity upon titration with electron-rich analytes (right); 1,3,5-trinitrobenzene (TNB), 2,4,6-trinitrotoluene (TNT), 2,4-dinitrotoluene (2,4-DNT), 3,4-dinitrotoluene (3,4-DNT), 3,5-dinitrobenzoic acid (3,5-DNBA), 3-nitrobenzoic acid (3-NBA), 4-nitrobenzoic acid (4-NBA), 4-nitrotoluene (4-NT), nitrobenzene (NB), 4-methoxybenzoic acid (4-MeO-BA), benzoic acid (BA), chlorobenzene (CB), and 1,2-dichlorobenzene (DCB or 1,2-DCB).

emission indicated that these MOFs are biased towards NACs and should therefore offer higher selectivity for the detection of nitro-explosives. Although **MOF-1** and **MOF-2** showed high selectivity towards all of the NACs with similar quenching efficiencies, **MOF-3** was especially selective for TNT, TNB, and DNTs, which are the main constituents of commonly used chemical explosives. An opposite effect was observed when the electron-rich analytes (*p*-xylene, 1,2-dichlorobenzene, and *p*-cresol) were added to the MOFs. Unlike NACs, these electron-rich analytes appeared to enhance the fluorescence intensity of the MOFs, as observed in a few previous cases.[18d,h] The fluorescence quenching and enhancement can be attributed to the donor–acceptor electron transfer between the MOFs and the analytes. Due to the extended network structure of the MOFs, they possess narrow energy bands because of highly localized electronic states, especially in the present cases involving d^{10} metal ions. As demonstrated by Li and co-workers,[18d] for an extended structure, calculation of electronic band structure is much more appropriate compared to molecular orbital (MO) calculations. Indeed, the valence band (VB) and conduction band (CB) energies can be described in a similar manner to the MOs of discrete molecules. One can envisage that electron-deficient analytes (e.g., nitroaromatics) will quench the luminescence of the MOFs if the lowest unoccupied MOs (LUMOs) of the analytes, which are π^*-type orbitals, reside between the VB and CB of the luminescent MOFs. Upon excitation, effective charge transfer can take place from the CB of the MOFs to the LUMO of the NACs, thereby quenching the fluorescence intensity. Hence, for more electron-deficient analytes with more stable LUMOs, electron transfer from the CB of a particular MOF to the LUMOs of the analytes becomes thermodynamically more favorable. However, with electron-rich analytes, for which the LUMO is located above the CB of the MOFs, excited-state electrons from the LUMO of the analytes will be transferred to the CB of the MOFs, leading to enhancement of the PL intensity.

The feasibility of the fluorescence quenching mechanism can be better understood by Rehm–Weller analysis according to Equation (1):

$$\Delta G^0 = E^{0(\mathrm{ox})}_{\mathrm{MOF}} - E^{0(\mathrm{red})}_{\mathrm{analyte}} - \Delta E_{00}(\mathrm{MOF}) \qquad (1)$$

where $E^{0(\mathrm{ox})}_{\mathrm{MOF}}$ is the oxidation potential of the MOF, $E^{0(\mathrm{red})}_{\mathrm{analyte}}$ is the reduction potential of the analyte, and ΔE_{00} is the difference in energy between the lowest vibrational levels of the excited state and the ground state of the MOF. $E^{0(\mathrm{ox})}_{\mathrm{MOF}}$ and $E^{0(\mathrm{red})}_{\mathrm{analyte}}$ were calculated with respect to the standard calomel electrode (SCE); ΔE_{00} was calculated from the absorption and emission spectra of the MOFs. The reduction potentials of all three MOFs and various analytes are given in Table S1 in the Supporting Information. It is noted that the free energy change (ΔG^0) associated with the electron-transfer process was determined to be negative, which is the driving force of the fluorescence quenching process for all of the MOFs (Table 2).

For a better understanding of the fluorescence quenching and enhancement mechanisms, we carried out density of states (DOS) calculations on the MOFs. The band gaps of **MOF-1** and **MOF-3** were calculated as 1.76 and 2.07 eV, respectively (Figure 7). A schematic diagram of the fluorescence quenching mechanism of the MOFs by a representative ana-

Table 2. Free energy changes (ΔG^0) associated with the fluorescence quenching processes.

MOFs	ΔG^0_{TNT} [kcal mol^{-1}]	$\Delta G^0_{2,4\text{-DNT}}$ [kcal mol^{-1}]	ΔG^0_{NB} [kcal mol^{-1}]	$\Delta G^0_{4\text{-NT}}$ [kcal mol^{-1}]
MOF-1	−26.46	−19.55	−16.09	−14.93
MOF-2	−24.26	−17.34	−13.88	−12.73
MOF-3	−14.60	−7.68	−4.22	−3.07

lyte, TNT, is shown in Figure 7c. Interestingly, the theoretical calculations indicated that the LUMO of TNT (−4.54 eV) is situated between the VB and CB of the MOFs. Hence, excited-state electron transfer would be expected from the CB of the MOFs to the LUMO of TNT, resulting in fluorescence quenching. Moreover, theoretical calculations on the same MOFs and a representative electron-rich analyte (*p*-xylene) showed that the excited-state electrons from the LUMO of *p*-xylene (located above the CBs of the MOFs; Figure 7) would be expected to populate the CB of the MOFs, resulting in fluorescence enhancement. Notably, the theoretical calculations are in accord with the experimental observations.

Although all of the MOFs showed high selectivity towards NACs, it was more important to determine the rate of quenching, which is essentially related to the Stern–Volmer constant (K_{SV}). Most previously reported studies related to MOFs for NAC detection have mainly been concerned with selectivity without any focus on quenching rate.[18] It is important to mention here that an effective sensing material must show a finite and measurable response to the analytes at a particular concentration. The rates of PL quenching of the MOFs by a few selected NACs are shown in Figure 8. To our surprise, the rates of quenching of **MOF-1** and **MOF-2** were faster with 2,4-DNT, 3,4-DNT, and 4-NT than with TNT and TNB, which was not fully in accordance with the trend of electron deficiency. With **MOF-3**, however, the rates of quenching followed the expected order, those with TNT and TNB being faster. This apparent anomaly could be clearly understood by detailed analysis of the experimental quenching mechanism, which was again supported by theoretical investigations. For this, we chose two extreme analytes, TNT and 4-NT, and the mechanisms were elaborated in detail. The quenching rate is determined by the Stern–Volmer

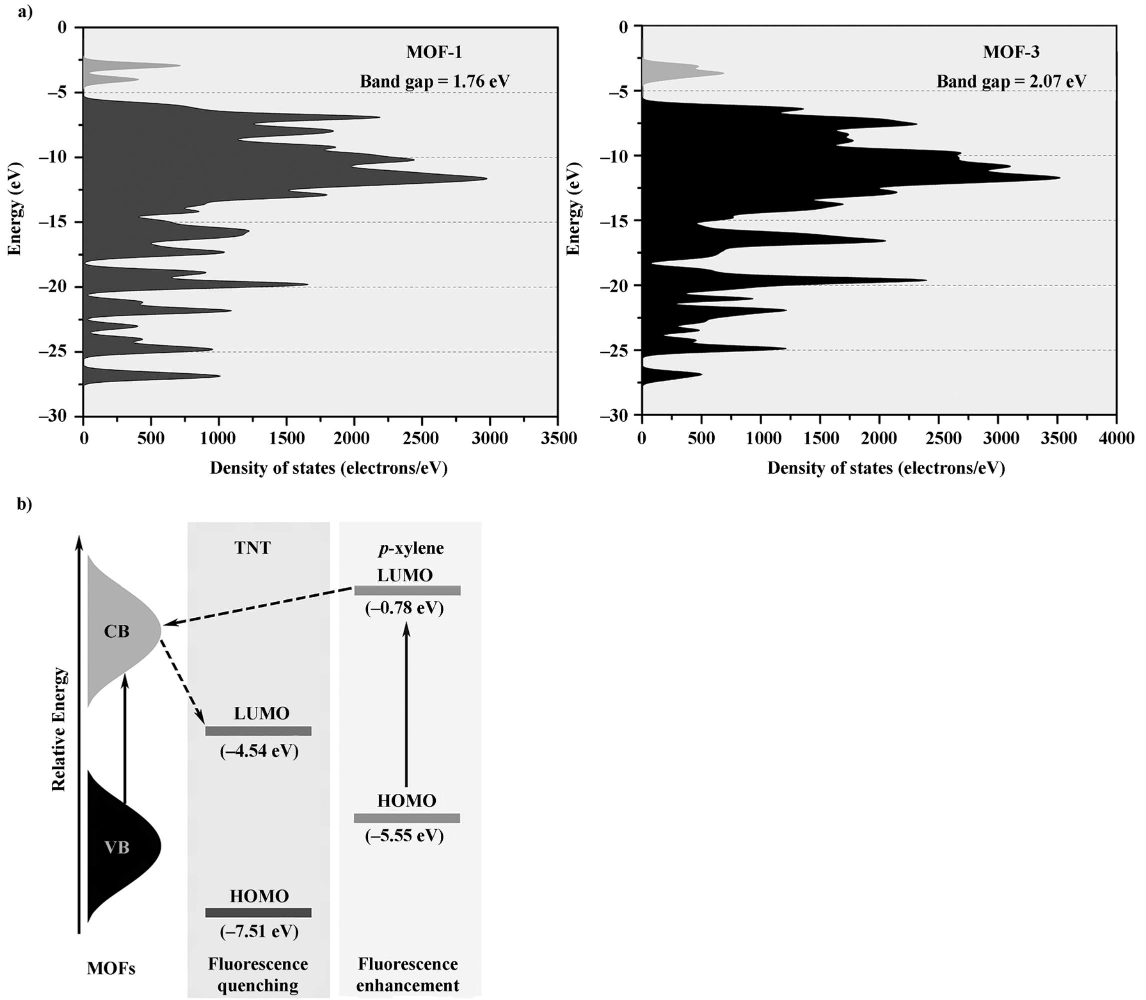

Figure 7. (a) The calculated densities of states of **MOF-1** and **MOF-3**. (b) Schematic representation of fluorescence quenching and enhancement mechanisms. The LUMO of TNT is located between the VB and the CB of the MOFs, leading to quenching. The LUMO of *p*-xylene is situated above the CB of the MOF, which is responsible for the fluorescence enhancement.

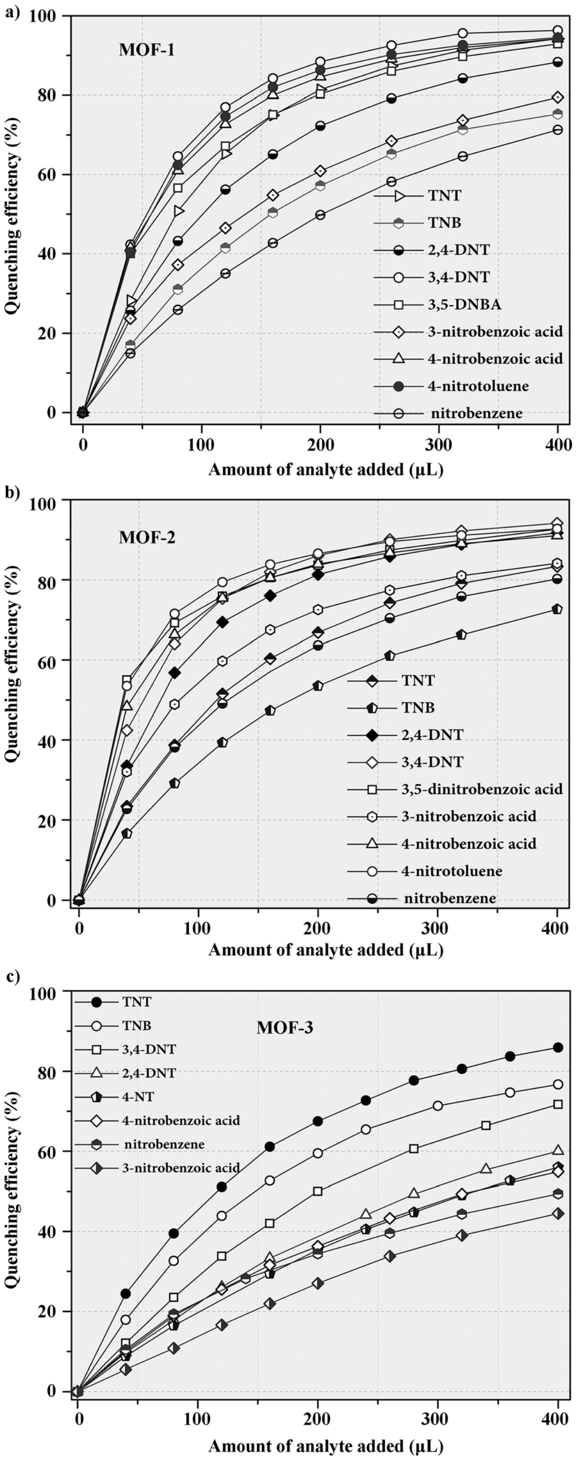

Figure 8. Rates of fluorescence quenching of (a) **MOF-1**, (b) **MOF-2**, and (c) **MOF-3** with selected nitroaromatics.

binding constant (K_{SV}), and in most cases it has been obtained from steady-state fluorescence quenching experiments.

If only one kind of quenching mechanism is operative, the quenching can be represented by the Stern–Volmer equation [Eq. (2)], where I_0 is the initial PL intensity before addition of the analyte, I is the PL intensity for any given concentration of quencher [Q], and K_{SV} is the Stern–Volmer constant.

$$\frac{I_0}{I} = 1 + K_{SV}[Q] \tag{2}$$

If the I_0/I versus [Q] plot is linear, K_{SV} can be estimated accurately. However, it does not give any insight into the quenching mechanism operating between the sensing material and analytes. Moreover, in most cases a plot of I_0/I versus [Q] deviates from linearity, which is typically due to the presence of two distinct quenching mechanisms. In static quenching, a non-emissive ground-state complex is formed between the fluorophore and quencher, whereas in dynamic quenching, electron transfer takes place between the analyte and quencher in the excited state through collisions. The two mechanisms can be differentiated by time-resolved measurements of PL decays of the sensing material at different analyte concentrations. If the PL lifetime of a sensor remains unchanged upon increasing addition of a quencher, the quenching mechanism is considered to be static. However, collisional quenching offers an additional relaxation pathway for the excited molecule and therefore reduces the PL lifetime.

To explore the quenching mechanism, the excited-state lifetimes of the MOFs were measured before and after multiple additions of 4-NT and TNT solutions. The decreases in the PL lifetimes of the MOFs upon addition of 4-NT and TNT suggested the presence of dynamic quenching. The lifetime decays were analyzed by the Stern–Volmer equation given by [Eq. (3)]:

$$\frac{\tau_0}{\tau} = 1 + K_C[Q] \tag{3}$$

where τ_0 is the PL lifetime of the MOF before addition of the analyte, τ is the PL lifetime of the MOF at a given analyte concentration [Q], and K_C is the Stern–Volmer collisional constant. Time-resolved Stern–Volmer plots for collisional quenching of the MOFs with 4-NT and TNT are shown in Figure 9. The values of the collisional constant K_C were extracted by fitting the plots using Equation (3). **MOF-1** showed the highest K_C values with both 4-NT and TNT, at 193 M^{-1} and 311 M^{-1}, respectively. For **MOF-2** and **MOF-3**, the values were much lower at 10.2 M^{-1}, 19.6 M^{-1} and 16.4 M^{-1}, 13.7 M^{-1}, respectively.

For steady-state PL quenching involving both static and collisional quenching, the change of fluorescence quenching is given by Equation (4):

$$\frac{I_0}{I} = (1 + K_C[Q])(1 + K_S[Q]) \tag{4}$$

which contains both collisional (K_C) and static (K_S) terms. The apparent deviation from linearity of the steady-state PL quenching can be rationalized by expanding the above equation [Eq. (5)].

$$\frac{I_0}{I} = 1 + K_C[Q] + K_S[Q] + K_CK_S[Q]^2 \tag{5}$$

When the analyte concentration is very low, the contribution of the $[Q]^2$ term is less prominent and Equation (5) would yield a linear plot. However, at higher concentrations, the plot deviates from linearity and the collisional constant (K_C) has a significant effect. The steady-state PL quenching data were fitted with Equation (5) using the collisional constants (K_C) obtained

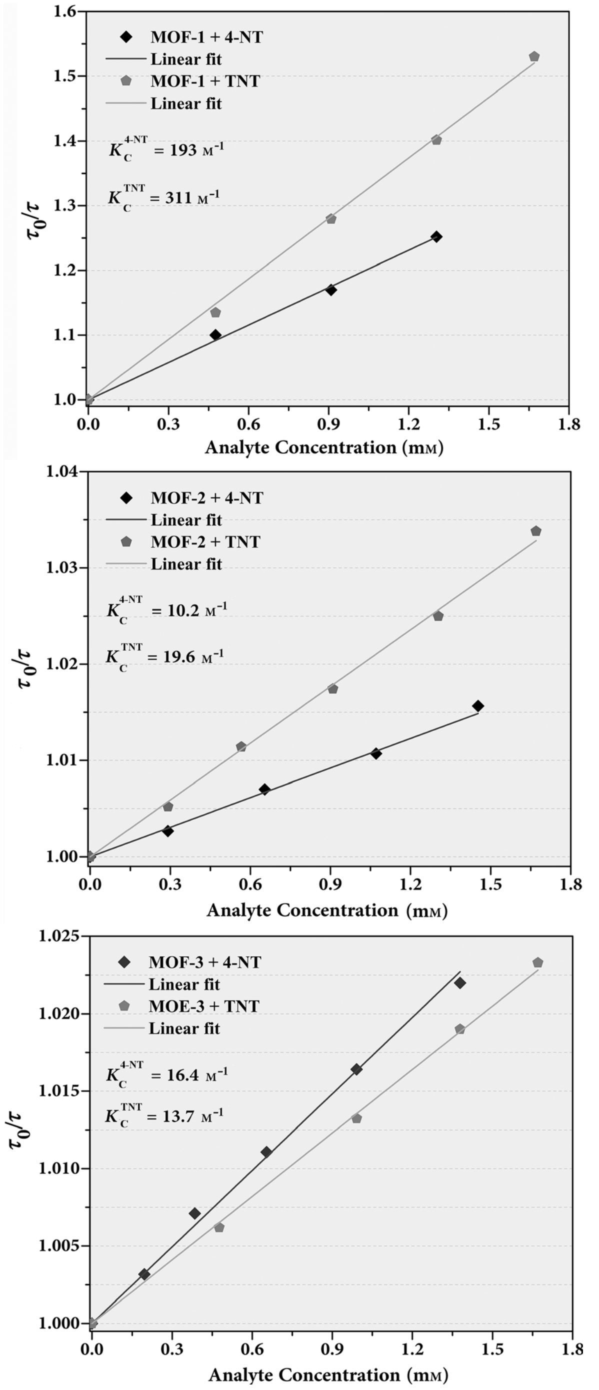

Figure 9. Time-resolved Stern–Volmer plots for **MOF-1**–**MOF-3** with 4-NT and TNT. The solid lines represent fits to the time-resolved data using Equation (2).

from the time-resolved experiments. The values of K_C and K_S for 4-NT and TNT with all of the MOFs are given in the corresponding Stern–Volmer plots. It is important to mention that the combination of K_C and K_S results in the Stern–Volmer constant (K_{SV}). The overall K_{SV} values for all of the MOFs with 4-NT and TNT are provided in Table 3.

The calculated static quenching constants (K_S) for **MOF-1** and **MOF-2** with 4-NT (5509 and 6855 M^{-1}, respectively) are much higher than those with TNT (2548 and 1535 M^{-1}, respectively; Figure 10). Surprisingly, the opposite trend was observed for **MOF-3** with $K_S = 563$ and 1611 M^{-1} for 4-NT and TNT, respectively. The abovementioned higher K_S for 4-NT is mainly responsible for the observed anomaly in the quenching rates of **MOF-1** and **MOF-2**. The extent of excited-state energy transfer depends on the distance between fluorophore and analyte, and becomes prominent when they are in close proximity. Thus, after excitation of the MOFs, the excited-state energy can migrate within the particle until it is completely dissipated by a radiative or nonradiative process. The energy migration within a particle is typically monitored by time-dependent fluorescence anisotropy decay analysis. This method can detect both molecular rotation as well as energy migration resonance energy transfer (EM-RET). For extended 3D MOFs, however, the fluorescence anisotropy decay by EM-RET is expected to be much faster than that by molecular rotation. The initial change in the slope of the anisotropy decay curves (Figure S12) of the MOFs in ethanol in the presence of TNT or 4-NT indicated energy migration within the particles.

Table 3. Lifetimes and Stern–Volmer constants. The Stern–Volmer constants were obtained by combining static and collisional quenching constants of the corresponding analytes.

MOFs	Lifetime [s]	$K_{SV}^{4\text{-NT}}$ [M^{-1}]	K_{SV}^{TNT} [M^{-1}]
MOF-1	9.3483×10^{-9}	5702	2859
MOF-2	1.2728×10^{-8}	6865.2	1554.6
MOF-3	2.1663×10^{-8}	579.4	1624.7

The experimentally observed static quenching phenomenon can be satisfactorily rationalized by band structure calculations of the free MOFs. If a nitroaromatic compound (with LUMO between the VB and the CB of the MOF) forms a ground-state charge-transfer complex with the MOF, the energy of the CB of the newly formed complex will be lowered, whereas the VBs would remain unchanged. The greater the electron deficiency of the analytes, the greater the lowering of the CB of the charge-transfer complex. This phenomenon is clearly reflected in the variation of the band gaps of the MOFs upon complexation with different electron-deficient analytes. The band gap of **MOF-1** (1.76 eV) gradually decreased upon the encapsulation of electron-deficient analytes. Theoretical studies indicated that the band gap for **MOF-1** decreased from 1.76 to 1.25 eV upon complexation with one 4-NT molecule per unit cell (Supporting Information), and further decreased to 1.21 eV with two 4-NT molecules per unit cell. A sharp decrease in the band gap (1.76 to 0.84 eV) was calculated when two 3,4-DNT molecules per unit cell were encapsulated into the pores of **MOF-1**. According to our calculations, the energy of the top of the VB of **MOF-1** remains almost unchanged (from −5.85 to −5.88 to −5.89 eV), whereas the energy of the CB lowers from −4.09 to −4.67 to −5.05 eV in the presence of two 4-NT and two 3,4-DNT molecules, respectively (Figure 11).

The experimentally determined higher K_S values for 4-NT compared to those for TNT with **MOF-1** and **MOF-2** may be attributed to the solvent-accessible porosity and pore width of

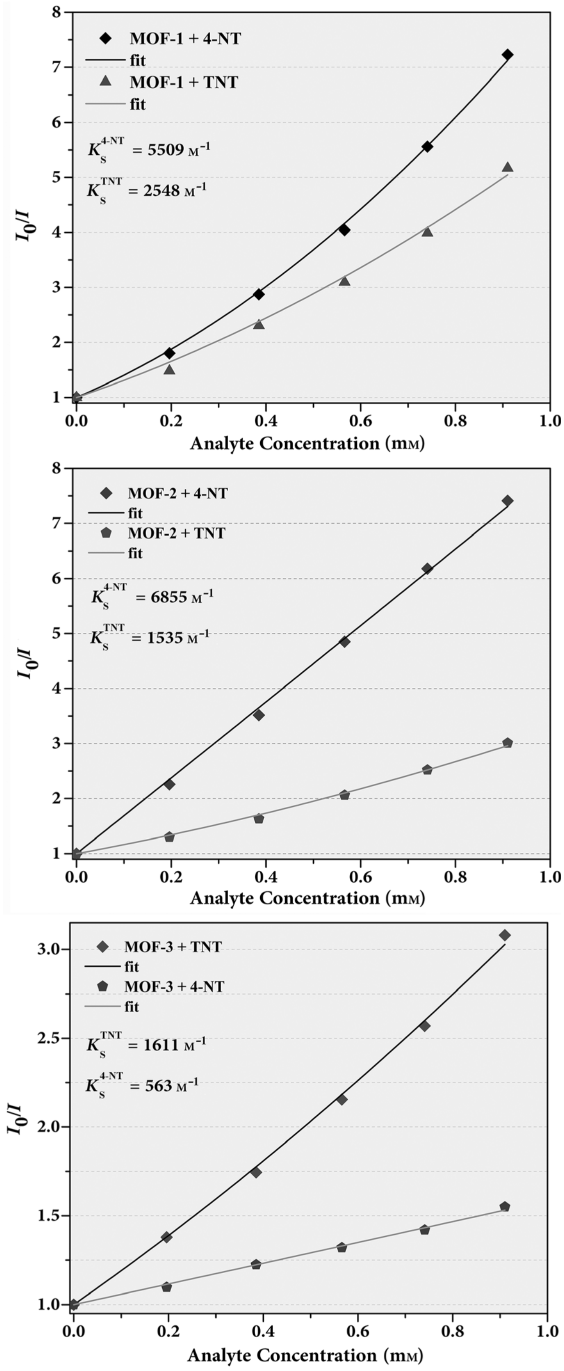

Figure 10. Steady-state Stern–Volmer plots for **MOF-1**–**MOF-3** with 4-NT and TNT. The solid lines represent fits to the steady-state data using Equation (3). The corresponding static quenching constants are given.

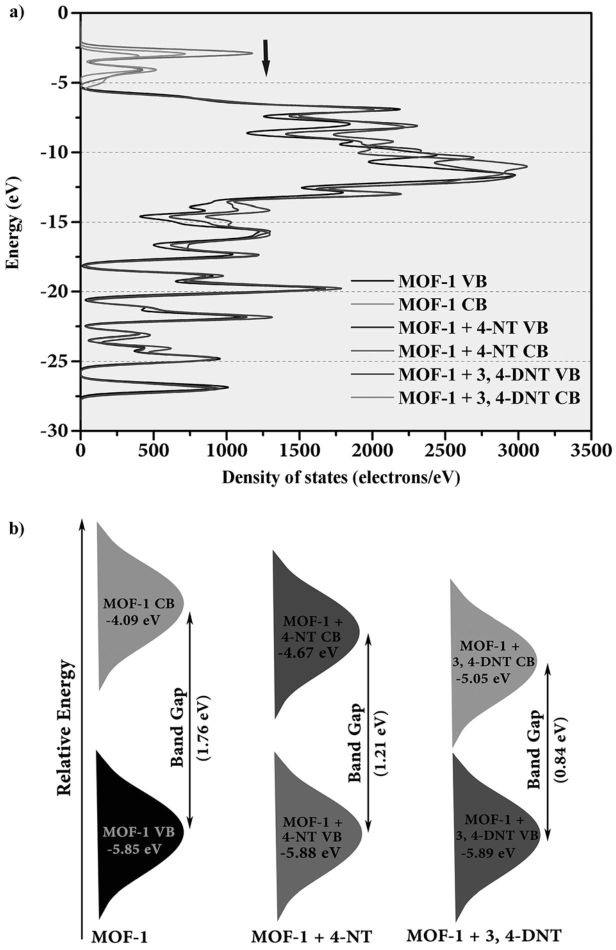

Figure 11. (a) Calculated superimposed plots of density of states of **MOF-1** along with the presence of two 4-NT and two 3,4-DNT molecules per unit cell of the **MOF-1**. The position of the VB of the **MOF-1** remains almost unchanged in the presence of the analytes. Lowering of the CB is observed in the presence of these analytes. (b) Schematic representation of the change of band gap in the presence of the abovementioned analytes.

the MOFs indicated by PLATON calculations as well as by BET surface area measurement. The PLATON calculations indicated that **MOF-1** (45%) had a higher solvent-accessible volume compared to **MOF-3** (9.8%). This was also reflected in the BET surface area measurements for all of the MOFs. Although all of the MOFs showed typical type II adsorption isotherms, **MOF-1** (217 $m^2 g^{-1}$) and **MOF-2** (185 $m^2 g^{-1}$) had higher surface areas than MOF **3** (37.6 $m^2 g^{-1}$) (Figure S15). The calculated pore diameters were 11 Å, 9 Å, and 2 Å for **MOF-1**–**MOF-3**, respectively. Thus, 4-NT can easily enter into the channels so as to better interact with the fluorescent tags (phenyl and naphthyl) in **MOF-1** and **MOF-2**. However, the larger size of TNT prevents it from entering the channels, thus resulting in lower K_S values. Thus, the observed fluorescence quenching of MOFs by the NACs can be attributed to two distinct features: (i) for **MOF-1** and **MOF-2**, the quenching process is mainly due to the encapsulation of smaller NAC molecules (4-NT, 2,4-DNT) over larger molecules (TNT), and (ii) for **MOF-3**, the process occurs primarily because of surface adsorption of the NACs on the MOF particles.

The apparently anomalous behavior and host (MOF)–guest (analyte) interaction could be adequately rationalized on the basis of theoretical optimization of the structures in the presence of various analytes. Due to the large number of atoms present in the unit cell of activated **MOF-1**, only one unit cell with periodic boundary conditions was considered for all of the calculations. Two 4-NT and 3,4-DNT molecules were randomly inserted into the cavity of the unit cell segment of the

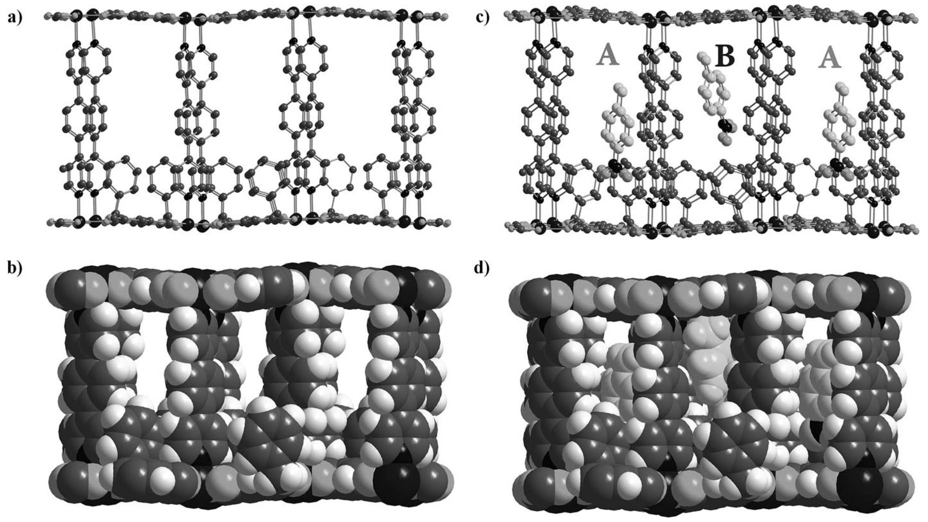

Figure 12. (a) Extended network view of **MOF-1** showing the presence of one-dimensional channel-like pores and (b) corresponding space-filling view, which clearly indicates that **MOF-1** can encapsulate small molecules through size selection. (c) Extended molecular view of **MOF-1** after accommodation of two 4-NT molecules inside the pores. Two types of 4-NT are present based on their positions, marked as **A** and **B**. Type **A** 4-NT molecules are very close to the phenyl tag, whereas type **B** 4-NT does not have much interaction with the phenyl ring. (d) Space-filling representation of 4-NT encapsulated in **MOF-1**.

activated **MOF-1** and a quantum mechanical geometry optimization was carried out to investigate the most favorable host–guest interactions. As we anticipated, 4-NT (as well as 3,4-DNT) interacted mainly with the fluorescent tag moiety (-Ph). The positions of the two 4-NT molecules were different (Figure 12), with one (marked as **A**) close to the -Ph tag, and the other (marked as **B**) not significantly interacting with the -Ph tag. A similar observation for the analyte 3,4-DNT (Supporting Information) indicated that this molecule could also be accommodated in the cavity of **MOF-1** during the fluorescence titration. However, similar calculations using TNT as the analyte indicated destabilization of the system. Hence, one may assume that the cavity of **MOF-1** cannot accommodate TNT or larger analytes. Thus, the observed fluorescence quenching of **MOF-1** with TNT can mainly be ascribed to surface interaction. Diffusion into the pores of **MOF-1** and **MOF-2** is controlled by the size of the analytes. Attempted geometry optimizations of **MOF-3** with 4-NT and 3,4-DNT were unsuccessful because the cavity of this MOF is almost occupied by the pyrenyl fluorescent tag, leaving insufficient space to accommodate a guest. An extended molecular network view is given in Figure 13, along with the corresponding space-filling model, to support this conjecture. The space-filling model clearly indicates a lack of molecular porosity in **MOF-3** due to the presence of the pyrenyl moieties. Thus, the observed fluorescence quenching phenomenon for **MOF-3** can only be due to an electronic effect. Therefore, as expected, the most electron-deficient analyte, TNT, exhibited the highest quenching rate. Hence, for **MOF-1** and **MOF-2** the fluorescence quenching takes place through size selection, whereas for **MOF-3** the quenching phenomenon follows the trend of the electron deficiencies of the NACs.

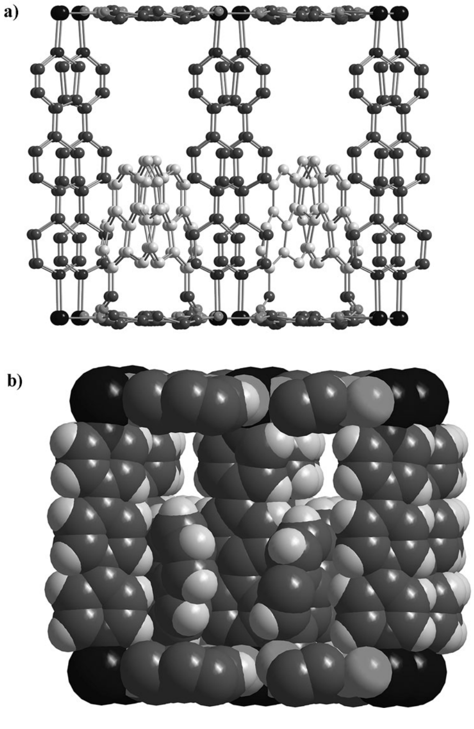

Figure 13. (a) Extended molecular representation of **MOF-3** and (b) corresponding space-filling model, which indicates that the pores are blocked by the pyrene moieties.

The faster quenching rates of **MOF-1** and **MOF-2** with 4-NT may be better understood on the basis of solvent-dependent PL quenching experiments. In a typical process, **MOF-1** was dispersed in cyclohexane in a similar manner as in ethanol and titrated with a solution of 4-NT in chloroform. A drastic change in the quenching rate with 4-NT was observed when **MOF-1** was dispersed in cyclohexane (Figure 14) instead of ethanol. A similar experiment with a solution of TNT in chloroform showed almost no change in the quenching rate upon using cyclohexane instead of ethanol. In cyclohexane, the rate of quenching with 4-NT was markedly decreased even though the quenching efficiency reached almost 80% upon addition of 400 μL of the analyte solution. This can be ascribed to the fact that the less polar nature of 4-NT makes it well solvated in cyclohexane such that it has less interaction with the MOF. However, in more polar ethanol, it is less solvated and may enter the almost nonpolar pores of the MOFs, interacting

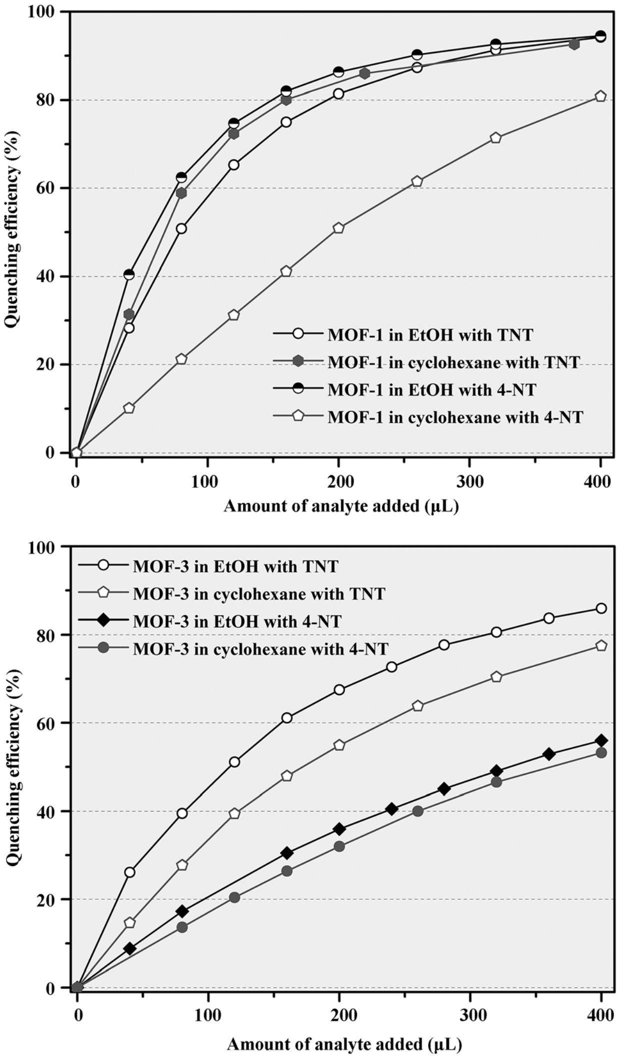

Figure 14. Solvent-dependent fluorescence quenching of **MOF-1** and **MOF-3** with 4-NT and TNT. A drastic change in fluorescence quenching rate was observed for **MOF-1** in the presence of 4-NT, but in the presence of TNT the rate remained almost unchanged (top). No prominent solvent effect was observed for **MOF-3** (bottom).

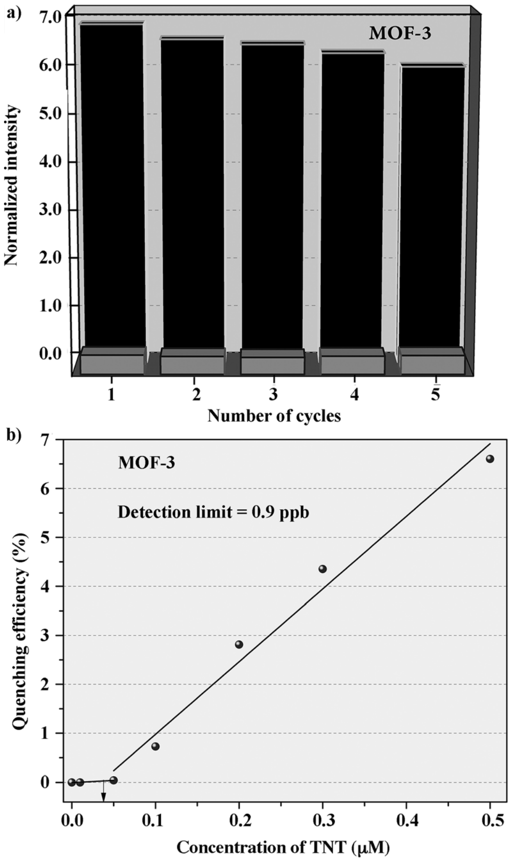

Figure 15. (a) Recyclability of **MOF-3** dispersed in ethanol for TNT detection. The MOF was filtered and washed several times with ethanol after each experiment. The black bars represent the initial fluorescence intensity and the grey bars represent the intensity upon addition of 400 μL of a 10 mM solution of TNT. (b) Determination of the detection limit of **MOF-3** towards TNT solution. The detection limit was calculated from the intercept of the two linear fits of the data.

more extensively with the fluorescent tags. A similar experiment on **MOF-3** revealed that the quenching rates were not significantly altered for either 4-NT or for TNT upon replacing the polar solvent (ethanol) with a less polar solvent (cyclohexane). This observation further implied that the quenching of the PL of **MOF-3** by nitroaromatics takes place through surface adsorption rather than by encapsulation.

The sensitivity of the MOFs towards TNT solution was found to be of the order of parts per billion (ppb). However, the sensitivity was higher for **MOF-3** (0.9 ppb) compared to the other two MOFs (3.63 ppb and 2.27 ppb for **MOF-1** and **MOF-2**, respectively; Figure 15). The detection limit for TNT with **MOF-3** falls below the permissible level of TNT in drinking water established by the US EPA.[7] Moreover, all of the MOFs could be reused over a significant number of cycles after repeated washing with ethanol. The almost complete recovery of the initial fluorescence intensity of all of the MOFs over several cycles implied their high photostability, making them potentially applicable for long-term in-field explosive detection or environmental monitoring applications.

As discussed above, all of the prepared MOFs were highly selective towards NACs over other aromatic compounds. However, in the present case, the rates of quenching not only depend on the electronic properties of the MOFs and analytes, but also on the porosity of the MOFs in relation to the size of the analytes. Since the examined fluorescence quenching mainly takes place through the static mechanism, **MOF-1** and **MOF-2** are better sensors for small NACs (less electron deficient) due to the their higher porosities. For **MOF-3**, however, the rates of quenching follow the order of the electron deficiencies of the analytes because in this case the quenching takes place through surface adsorption on the MOF particles. Sensitivity studies showed that **MOF-3** was able to sense TNT at a level as low as 0.9 ppb, much lower than with **MOF-1** and **MOF-2**. The order of sensitivity from **MOF-1** (3.63 ppb) to **MOF-3** (0.9 ppb) indicates that a more electron-rich MOF prefers more electron-deficient NACs over less electron-deficient analytes. Thus, by tuning the porosity as well as increasing the electron density of the MOFs, we may be able to discriminate NACs and increase the sensitivity towards TNT.

Conclusion

In conclusion, three new luminescent Zn-MOFs have been synthesized by employing new isophthalic acid derivatives bearing aromatic tags with different degrees of π-conjugation. The ligands consist of two distinct functionalities: the dicarboxylate moiety for assembly of the coordination polymer and the attached aromatic tags to enhance the electron density into MOFs. The aromatic tags were used strategically to enhance the electron density of the MOFs for the detection of NACs. Dispersions of the MOFs in ethanol exhibited strong fluorescence emissions, but their initial PL intensities were efficiently quenched upon addition of a small amount of a nitroaromatic explosive. Our study has revealed that all of the prepared MOFs were highly selective towards explosive nitroaromatics such as DNT, TNT, and TNB over the other electron-deficient aromatics. However, the rates of quenching of **MOF-1** and **MOF-2** were higher with DNT and 4-NT compared to those with TNT and TNB, whereas **MOF-3** showed a quenching order in accordance with that expected based on the electron deficiencies of the analytes. This apparent anomaly in quenching rates has been fully investigated by the determination of static quenching constants (K_S) as well as collisional quenching constants (K_C) from steady-state PL titration and time-resolved PL decays, respectively. The experimental observations have been well corroborated by theoretical studies. Moreover, the recyclability and very high sensitivity of the MOFs towards TNT make them potential sensors for the detection of NACs. Thus, this methodology of designing electron-rich fluorescent MOFs for the selective and efficient sensing of electron-deficient NAC explosives and complete investigation of the quenching mechanism may enable the discovery of a new generation of much improved sensors for in-field explosives sensing.

Experimental Section

Materials and methods

All chemicals and solvents were obtained from commercial sources and were used without further purification, unless otherwise mentioned. 1-(Bromomethyl)naphthalene, 1-(bromomethyl)pyrene, and 1,4-di(pyridin-4-yl)benzene were prepared according to the relevant literature procedures.[27] NMR spectra were recorded on a Bruker 400 MHz spectrometer. Chemical shifts (δ) in the ^{1}H NMR spectra are reported in ppm relative to tetramethylsilane (TMS) as an internal standard ($\delta = 0.0$ ppm). IR spectra were recorded on a Bruker ALPHA FTIR spectrometer over the range 4000–400 cm^{-1}. Elemental analyses were carried out on a Perkin-Elmer 240C CHNS analyzer. Powder X-ray diffraction (XRD) data were recorded on a Philips X'pert Pro using Cu$_{K\alpha}$ radiation ($\lambda = 1.5406$ Å). Thermogravimetric (TG) analyses of the MOFs were carried out on a Mettler-Toledo thermal gravimetric analyzer under a nitrogen flow. Electronic absorption spectral measurements were performed on a Perkin-Elmer Lambda 750 UV/Vis spectrophotometer and fluorescence emission studies were carried out on a Horiba Jobin Yvon Fluoromax-4 spectrometer. Lifetime analyses were carried out on a Horiba Scientific DAS6 instrument using spectroscopic grade solvents.

Synthesis

Dimethyl 5-(benzyloxy)isophthalate (1): A two-necked flask was charged with dimethyl 5-hydroxyisophthalate (992.9 mg, 4 mmol), potassium carbonate (1658.0 mg, 12 mmol), and potassium iodide (663.5 mg, 4 mmol) under a nitrogen atmosphere, and then dry acetonitrile (60 mL) was added. Finally, benzyl bromide (821.0 mg, 4.8 mmol) was added dropwise by means of a syringe. The reaction mixture was stirred at reflux under nitrogen for 24 h. The solvent was then removed under vacuum and the residue was dried completely. The crude product was partitioned between dichloromethane and water. The organic phase was washed three times with brine, dried over anhydrous Na_2SO_4, filtered, and concentrated under reduced pressure. The crude product was purified by column chromatography on silica gel (60–120 mesh) eluting with chloroform/hexane (1:1) to afford compound **1** as a white crystalline solid (85% yield). ^{1}H NMR ($CDCl_3$): $\delta = 8.291$ (d, 1H), 7.839 (d, 2H), 7.461–7.343 (m, 5H), 5.145 (s, 1H), 3.936 ppm (s, 6H); ^{13}C NMR ($CDCl_3$): $\delta = 166.542$, 159.222, 136.497, 132.254, 129.122, 128.703, 128.017, 123.661, 120.614, 70.912, 52.873 ppm.

5-(Benzyloxy)isophthalic acid (H_2L^1) (2): Dimethyl 5-(benzyloxy)-isophthalate (1201.0 mg, 4 mmol) was taken up in MeOH/H_2O (1:1, v/v; 50 mL) in a round-bottomed flask. NaOH (480 mg, 12 mmol) was then added and the mixture was heated at reflux for 12 h. The clear solution was then concentrated under vacuum, cooled to room temperature, and filtered. The aqueous phase was acidified with dilute hydrochloric acid to afford a white solid, which was collected by filtration, washed several times with distilled water, and finally dried under vacuum. Yield: 95%. FTIR: $\tilde{\nu} = 2828$ (w), 2537 (w), 1689 (w), 1594 (m), 1461 (m), 1431 (s), 1313 (s), 1275 (s), 1118 (w), 1027 (s), 942 (s), 907 (m), 839 (w), 755 (s), 731 (w), 694 (s), 667 (w), 610 (m), 549 (w), 505 (m), 437 cm^{-1} (w); ^{1}H NMR ([D$_6$]DMSO): $\delta = 13.297$ (s, 2H), 8.091 (s, 1H), 7.738 (d, 2H), 7.490 (d, 2H), 7.391 (m, 2H), 7.343 (d, 1H), 5.244 ppm (s, 2H); ^{13}C NMR ([D$_6$]DMSO): $\delta = 167.272$, 159.377, 137.421, 133.530, 129.404, 128.872, 128.539, 123.347, 120.371, 70.588 ppm.

Dimethyl 5-(naphthalen-1-ylmethoxy)isophthalate (3): A two-necked flask was charged with dimethyl 5-hydroxyisophthalate (496.5 mg, 2 mmol), potassium carbonate (829.3 mg, 6 mmol), and potassium iodide (331.7 mg, 2 mmol) under a nitrogen atmosphere, and then dry acetonitrile (30 mL) was added. 1-(Bromomethyl)naphthalene (530.6 mg, 2.4 mmol) was then added dropwise and the resulting mixture was heated under reflux for 24 h with stirring. Thereafter, the solvent was removed under vacuum and the crude product was extracted with ethyl acetate. The organic phase was washed three times with brine, dried over anhydrous Na_2SO_4, and concentrated to dryness. The crude product was purified by column chromatography on silica gel (60–120 mesh) eluting with ethyl acetate/hexane (1:9). The pure product was obtained as a white solid (80% yield). ^{1}H NMR ($CDCl_3$): $\delta = 8.332$ (s, 1H), 8.044 (d, 1H), 7.925 (d, 2H), 7.895 (m, 2H), 7.631 (d, 1H), 7.553 (m, 2H), 7.482 (m, 1H), 5.575 (s, 2H), 3.942 ppm (s, 6H); ^{13}C NMR ($CDCl_3$): $\delta = 166.546$, 159.304, 134.251, 132.349, 131.951, 131.883, 129.813, 129.200, 127.311, 127.062, 126.466, 125.716, 124.034, 123.794, 120.662, 69.648, 52.887 ppm.

5-(Naphthalen-1-ylmethoxy)isophthalic acid (H_2L^2) (4): Dimethyl 5-(naphthalen-1-ylmethoxy)isophthalate (**3**; 700.7 mg, 2 mmol) was taken up in MeOH/H_2O (1:1, v/v; 50 mL) in a round-bottomed flask. NaOH (200 mg, 5 mmol) was then added and the mixture was heated at reflux for 12 h. The clear solution was then concentrated under vacuum, cooled to room temperature, and filtered. The aqueous phase was acidified with dilute hydrochloric acid to afford a white solid, which was collected by filtration, washed several times with distilled water, and finally dried under vacuum. Yield: 95 %. FTIR: $\tilde{\nu} = 2822$ (w), 2543 (w), 1686 (s), 1592 (s), 1462 (m), 1421 (s), 1319 (m), 1279 (s), 1128 (w), 1071 (s), 1011 (w), 908 (s), 878 (s), 787 (s), 758 (s), 693 (s), 659 (m), 615 (w), 565 (w), 525 (s), 483 cm^{-1} (m); ^1H NMR ([D_6]DMSO): $\delta = 13.325$ (s, 2 H), 8.141 (d, 1 H), 8.124 (d, 1 H), 7.999 (m, 2 H), 7.830 (d, 2 H), 7.710 (d, 1 H), 7.620 (m, 3 H), 5.698 ppm (s, 2 H); ^{13}C NMR ([D_6]DMSO): $\delta = 167.306$, 159.474, 134.210, 133.583, 132.894, 132.013, 129.765, 129.399, 127.723, 127.435, 126.946, 126.298, 124.871, 123.458, 120.485, 69.307 ppm.

Dimethyl 5-(pyren-1-ylmethoxy)isophthalate (5): An oven-dried, two-necked flask was charged with dimethyl 5-hydroxyisophthalate (462.4 mg, 2.2 mmol), potassium carbonate (829.3 mg, 6 mmol), and potassium iodide (364.9 mg, 2.2 mmol) under a nitrogen atmosphere, and then dry acetonitrile (30 mL) was added. 1-(Bromomethyl)pyrene (590.3 mg, 2 mmol) was added in one portion and the resulting mixture was stirred under nitrogen at reflux for 24 h. The solvent was then removed under vacuum and the residue was dried completely. The crude product was partitioned between ethyl acetate and water. The organic phase was washed three times with brine, dried over anhydrous Na_2SO_4, filtered, and concentrated under reduced pressure in a rotary evaporator. The crude product was purified by column chromatography on silica gel (60–120 mesh) eluting with ethyl acetate/hexane (1:9) to afford compound **5** as a white solid (80 % yield). ^1H NMR ($CDCl_3$): $\delta =$ 8.333 (s, 1 H), 8.286 (d, 1 H), 8.229 (m, 3 H), 8.209 (d, 2 H), 8.167 (m, 2 H), 8.048 (m, 1 H), 7.976 (d, 2 H), 5.812 (s, 2 H), 3.944 ppm (s, 6 H); ^{13}C NMR ($CDCl_3$): $\delta = 166.587$, 159.371, 132.369, 132.235, 131.671, 131.174, 129.832, 129.232, 128.720, 128.298, 127.819, 127.452, 126.572, 126.014, 125.416, 125.117, 123.850, 123.325, 120.750, 69.795, 52.919 ppm.

5-(Pyren-1-ylmethoxy)isophthalic acid (H_2L^3) (6): Dimethyl 5-(pyren-1-ylmethoxy)isophthalate (**5**; 500 mg, 1.2 mmol) was taken up in MeOH/H_2O (1:1, v/v; 50 mL) in a round-bottomed flask. NaOH (240 mg, 6 mmol) was then added and the mixture was heated to reflux for 12 h. The clear solution was then concentrated under vacuum, cooled to room temperature, and filtered. The aqueous phase was acidified with dilute hydrochloric acid to afford a pale-yellow solid, which was collected by filtration, washed several times with distilled water, and finally dried under vacuum. Yield: 95 %. FTIR: $\tilde{\nu} = 2845$ (w), 2634 (w), 1696 (s), 1592 (s), 1459 (m), 1412 (m), 1269 (s), 1181 (m), 1122 (m), 1067 (m), 1040 (m), 908 (m), 877 (m), 837 (s), 753 (s), 692 (s), 661 (m), 617 (w), 582 (w), 517 (w), 483 (w), 454 cm^{-1} (w); ^1H NMR (CD_3OD): $\delta = 13.290$ (s, 2 H), 8.211 (m, 3 H), 8.162–7.983 (m, 7 H), 7.753 (s, 2 H), 5.755 ppm (s, 2 H); ^{13}C NMR ([D_6]DMSO): $\delta = 167.464$, 159.267, 133.367, 131.819, 131.455, 130.952, 130.162, 129.540, 128.829, 128.529, 128.118, 127.348, 126.464, 126.379, 125.519, 124.763, 124.479, 123.900, 123.453, 120.573, 69.318 ppm.

Synthesis of MOF-1: $Zn(NO_3)_2 \cdot 6H_2O$ (6 mg, 0.02 mmol), H_2L^1 (5.5 mg, 0.02 mmol), and 1,4-di(pyridin-4-yl)benzene (4.6 mg, 0.02 mmol) were placed in an 8 mL scintillation vial. DMF (3 mL) was added and the mixture was stirred for 10 min at room temperature. The vial was then tightly capped, placed in a programmable oven, and heated at 120 °C for 24 h. It was then slowly cooled to room temperature at a rate of 15 °C h^{-1}. Colorless crystals of the product (10 mg, 88 %) were collected by filtration and washed with fresh DMF (2 × 3 mL). FTIR: $\tilde{\nu} = 3060$ (w), 2336 (m), 2064 (w), 2023 (w), 1961 (w), 1700 (s), 1606 (s), 1553 (s), 1444 (m), 1374 (s), 1310 (m), 1254 (m), 1119 (w), 1030 (s), 850 (m), 785 (s), 715 (s), 615 (w), 588 (w), 486 cm^{-1} (m); elemental analysis calcd (%) for $C_{31}H_{22}N_2O_5Zn$ [L^1Zn(dpb)] (activated sample): C 65.56, H 3.90, N 4.93; found: C 65.23, H 3.45, N 5.12.

Synthesis of MOF-2: $Zn(NO_3)_2 \cdot 6H_2O$ (6 mg, 0.02 mmol), H_2L^2 (6.5 mg, 0.02 mmol), and 1,4-di(pyridin-4-yl)benzene (4.6 mg, 0.02 mmol) were placed in an 8 mL scintillation vial. DMF (3 mL) was added and the mixture was stirred for 10 min at room temperature. The reaction vial was then tightly capped, placed in a programmable oven, and heated at 120 °C for 24 h. It was then slowly cooled to room temperature at a rate of 15 °C h^{-1}. Colorless crystals of the product (11 mg, 89 %) were collected by filtration and washed with fresh DMF (2 × 3 mL). FTIR: $\tilde{\nu} = 2355$ (s), 2179 (w), 2142 (w), 2046 (w), 1551 (s), 1448 (m), 1370 (s), 1224 (s), 1125 (w), 1061 (w), 1024 (m), 782 (s), 718 (s), 545 (w), 463 cm^{-1} (m); elemental analysis calcd (%) for $C_{35}H_{24}N_2O_5Zn$ [L^2Zn(dpb)] (activated sample): C 68.03, H 3.91, N 4.53; found: C 68.53, H 3.74, N 4.42.

Synthesis of MOF-3: $Zn(NO_3)_2 \cdot 6H_2O$ (6 mg, 0.02 mmol), H_2L^3 (7.9 mg, 0.02 mmol), and 1,4-di(pyridin-4-yl)benzene (4.6 mg, 0.02 mmol) were placed in an 8 mL scintillation vial. DMF (3 mL) was added and the mixture was stirred for 10 min at room temperature. The reaction vial was then tightly capped, placed in a programmable oven, and heated at 120 °C for 24 h. It was then slowly cooled to room temperature at a rate of 15 °C h^{-1}. Colorless crystals of the product (8 mg, 58 %) were collected by filtration and washed with fresh DMF (2 × 3 mL). FTIR: $\tilde{\nu} = 2362$ (s), 2330 (s), 2202 (s), 1995 (m), 1873 (w), 1605 (m), 1555 (s), 1371 (s), 1228 (m), 1123 (w), 1026 (m), 847 (m), 795 (s), 717 (s), 675 (m), 609 (w), 487 cm^{-1} (w); elemental analysis calcd (%) for $C_{41}H_{26}N_2O_5Zn$[L^3Zn(dpb)] (activated sample): C 71.16, H 3.79, N 4.05; found: C 71.52, H 4.02, N 4.41.

X-ray crystallographic data collection and refinements

Suitable X-ray diffraction quality single crystals of **MOF-1** and **MOF-3** were obtained by solvothermal reaction of the corresponding ligands and $Zn(NO_3)_2 \cdot 6H_2O$. The single crystals slowly lost their crystalline nature when removed from their mother liquors. Though we examined the crystals at low temperature (90 K), the quality of the collected diffraction data was less than satisfactory. **MOF-1** and **MOF-3** (CCDC-947143 and -947144) crystallized in the triclinic crystal system with the *P*1 space group and the orthorhombic crystal system with the *Pba*2 space group, respectively. The diffraction data of both the complexes were collected on a Bruker Kappa CCD diffractometer with $Mo_{K\alpha}$ radiation ($\lambda = 0.71073$ Å). Data reduction was carried out using the SMART/SAINT program.[28] The SADABS program was used for empirical absorption correction.[29] The structures were solved by direct methods (SHELXS-97) and standard Fourier techniques, and refined against F^2 by full-matrix least-squares procedures (SHELXL-97) implemented in WinGX.[30,31] All hydrogen atoms were assigned idealized positions and given thermal parameters equivalent to either 1.5 (methyl hydrogen atoms) or 1.2 (all other hydrogen atoms) times the thermal parameter of the carbon atom to which they were attached. The relatively high values of *R*(int.) and *R*(sigma) are due to the weak diffraction of the crystals. The aromatic rings in the 1,4-di(pyridin-4-yl)benzene, phenyl, and pyrene moieties (the tags) remained thermally disordered. Several atoms were refined with partial anisotropy. A few atoms in the **MOF-1** were refined isotropically due to the high disorder. Several fragments in the main structure deviate from their ideal geometry owing to high thermal vibration, thus leading to a high U_{iso}(max)/U_{iso}(min) ratio for non-solvent H atoms (10.0) upon affixation of H atoms to complete the models of the electronic structures. Weak diffraction strength and high thermal vibration led to relatively low C–C bond precision (as low as 0.2249 Å for **MOF-3** and 0.0259 Å for **MOF-1**). The solvent molecules are thermally too disordered to be located and hence, squeezed out completely from **MOF-1** using PLATON software. While one DMF molecule is located in the structure of **MOF-1** and rest of the solvents are squeezed out. The squeezed out solvents may comprise of DMF and water. Solvent-accessible void volumes predicted using PLATON software amounted to 1802 $Å^3$ and 399 $Å^3$ for **MOF-1** and **MOF-3**, respectively. The weak diffraction and high thermal distortion can be attributed to fact that the crystals decayed by losing crystallization solvents when taken out of mother liquor, even at low temperatures. Moreover, the large-framework cavities allowed dislocation of the crystallization solvent molecules and flipping of the conformationally flexible fragments (especially the fluorescent tags) of the structures. The refined crystallographic parameters are given in Table 1.

Activation of the MOFs

As-synthesized MOF samples (about 200 mg) were soaked in methanol and the supernatant was discarded at intervals of 8 h (three times) and replaced by fresh methanol. After methanol exchange, the sample was further treated in the same way with acetone and dichloromethane to remove methanol and acetone, respectively. Finally, the dichloromethane was decanted off and the sample was dried under a dynamic vacuum at 120 °C for 6 h.

Fluorescence quenching titrations in dispersed medium

The fluorescence properties of **MOF-1**–**MOF-3** were investigated in ethanol emulsions at 293 K. A stock suspension was prepared by dispersing MOF powder (3 mg) in ethanol (3 mL). For fluorescence measurements, 1 mL of the stock suspension was diluted to 2 mL with fresh ethanol, sonicated for 30 min, and subsequently placed in a quartz cell of pathlength 1 cm. All titrations were carried out by gradually adding methanolic solutions of the aromatic analytes (10 mм) in an incremental fashion. Each titration was repeated at least three times to obtain reliable titres. For all measurements, the excitation wavelengths (λ_{ex}) were 310 nm for **MOF-1**, 300 nm for **MOF-2**, and 360 nm for **MOF-3**. The corresponding emissions were monitored over the wavelength ranges λ_{em} = 320–600 nm for **MOF-1**, 310–600 nm for **MOF-2**, and 380–700 nm for **MOF-3**. Both the excitation and emission slit widths were 2 nm for all measurements. No change in shape of the emission spectra was observed upon gradual addition of the quenchers; only quenching of the initial fluorescence emission intensity occurred upon titration with electron-deficient nitroaromatic quenchers, whereas fluorescence enhancement was obtained with electron-rich analytes. To check the selectivity of the MOFs, aliquots (400 μL) of 10 mм solutions of each quencher were added to the MOFs dispersed in ethanol. The fluorescence efficiency was calculated according to $[(I_0-I)/I_0]\times 100\%$, where I_0 is the initial fluorescence intensity. The PL decays were fitted with double exponential convolved with instrumental reference. The recyclability of the MOFs for TNT-sensing was checked. As above, the fluorescence of the MOFs was recorded from dispersions in ethanol. An aliquot (400 μL) of a 1×10^{-3} м TNT solution was added to the dispersion and the fluorescence was measured once more. The material was recovered by centrifugation after each quenching experiment, washed several times with ethanol, dried, and reused for further cycles. For sensitivity measurements, a 10 μм TNT solution was gradually added to the MOFs dispersed in ethanol. Initially, the fluorescence intensity of the MOFs did not change, but with further addition of the substrate quenching was observed. The detection limit was calculated from the intercept of the two linear fits of the data.

Electrochemistry

The reduction potentials of the three MOFs and selected analytes were measured using a three-electrode cell at room temperature. An indium tin oxide (ITO) electrode was used as the working electrode, platinum as the counter-electrode, and a standard calomel electrode (SCE) as the reference. Electrochemical measurements of the analytes were carried out using 0.01 mм solutions of each in 1:1 acetonitrile/1.0 м aqueous tetrabutylammonium nitrate solution. For the MOFs, the powdered materials were coated on ITO electrodes. The reduction potentials of the compounds were obtained from the cyclic voltammograms and corrected with respect to the SCE.

Computational details

First principles DFT calculations were carried out by using the DMOL 3 module implemented in Accelrys.[32–34] The unit cells of **MOF-1** and **MOF-3**, with and without analytes, were optimized using a local density approximation with Perdew–Wang correlation (LDA/PWC) functional. A double numerical basis set with d polarization (DND), which is comparable to the 6–31G* basis set, was used for all calculations. A Fermi smearing of 0.005 Hartree was employed to improve the computational performance. The convergence criteria for energy, gradient, and displacement were 2.0×10^{-5} Hartree, 4.0×10^{-3} Hartree $Å^{-1}$, and 5.0×10^{-3} Å, respectively. The self-consistent field convergence criterion for all calculations was 1.0×10^{-5}. The projected density of states (PDOS) was calculated for the optimized structures.

Acknowledgements

P.S.M. thanks the IISc-STC for financial support. B.G. sincerely thanks Dibyendu Mallick for his assistance with the theoretical calculations. B.G. also thanks the Indian Institute of Science for a Bristol Mayer Squibb fellowship and research grant. A.K.B. thanks Rajat Saha for discussion on the crystal structures.

Keywords: coordination polymers · explosives sensing · fluorescence quenching · metal–organic frameworks · nitroaromatics · sensors · zinc(II) complexes

[1] W. C. Trogler, in *NATO ASI Workshop, Electronic Noses & Sensors for the Detection of Explosives* (Eds.: J. W. Gardner, J. Yinon), Kluwer Academic Publishers, Dordrecht, The Netherlands, **2004**.

[2] a) J. Yinon, in *Forensic and Environmental Detection of Explosives*, John Wiley & Sons, Chichester, **1999**; b) S. J. Toal, W. C. Trogler, *J. Mater. Chem.* **2006**, *16*, 2871–2883.

[3] a) A. W. Czarnik, *Nature* **1998**, *394*, 417–418; b) L. C. Shriver-Lake, B. L. Donner, F. S. Ligler, *Environ. Sci. Technol.* **1997**, *31*, 837–841; c) J. Lu, Z. Zhang, *Anal. Chim. Acta* **1996**, *318*, 175–179; d) M. Dock, M. Fisher, C. Cumming, in *Fifth International Symposium of Mine Warfare Association*, Monterey, CA, **2002**, pp. 1–5; e) V. George, T. F. Jenkins, D. C. Leggett,

J. H. Cragin, J. Phelan, J. Oxley, J. Pennington, *Proc. SPIE* **1999**, *3710*, 258–269.

[4] a) J. H. Fletcher, J. Hamilton, I. Hechenbleikner, E. Hoegberg, B. J. Sertl, J. Cassaday, *J. Am. Chem. Soc.* **1950**, *72*, 2461–2464; b) G. W. Ware, *The Pesticide Book*, Thomson Publications, Fresno, CA, **2000**; c) D. C. Leggett, T. F. Jenkins, R. P. Murrmann, *US Army Engineer Research and Development Center*, CRREL, **1977**, Special Report 77; d) R. Dalpozzo, G. Bartoli, *Curr. Org. Chem.* **2005**, *9*, 163–178.

[5] G. R. Lotufo, J. D. Farrar, L. S. Inouye, T. S. Bridges, D. B. Ringelberg, *Environ. Toxicol. Chem.* **2001**, *20*, 1762–1771.

[6] a) *Toxicological Profile for 2,4,6-Trinitrotoluene*, Agency for Toxic Substances and Disease Registry, US Department of Health and Human Services, Atlanta, GA, **1995**.

[7] *2004 Edition of the Drinking Water Standards and Health Advisories*, US Environmental Protection Agency, Washington DC, **2004**.

[8] *Approaches for the Remediation of Federal Facility Sites Contaminated with Explosive or Radioactive Wastes*, US Environmental Protection Agency, Washington DC, **1993**.

[9] a) D. S. Moore, *Rev. Sci. Instrum.* **2004**, *75*, 2499–2512; b) G. E. Spangler, J. Carrico, D. Campbell, *J. Test. Eval.* **1985**, *13*, 234–240; c) L. M. Dorozhkin, V. A. Nefedov, A. G. Sabelnikov, V. G. Sevastjanov, *Sens. Actuators B* **2004**, *99*, 568–570; d) E. S. Forzani, D. L. Lu, M. J. Leright, A. D. Aguilar, F. Tsow, R. A. Iglesias, Q. Zhang, J. Lu, J. H. Li, N. J. Tao, *J. Am. Chem. Soc.* **2009**, *131*, 1390–1391; e) R. A. McGill, T. E. Mlsna, R. Chung, V. K. Nguyen, J. Stepnowski, *Sens. Actuators B* **2000**, *65*, 5–9.

[10] a) K. Håkansson, R. V. Coorey, R. A. Zubarev, V. L. Talrose, P. Hakansson, *J. Mass Spectrom.* **2000**, *35*, 337–346; b) J. M. Sylvia, J. A. Janni, J. D. Klein, K. M. Spencer, *Anal. Chem.* **2000**, *72*, 5834–5840; c) V. P. Anferov, G. V. Mozjoukhine, R. Fisher, *Rev. Sci. Instrum.* **2000**, *71*, 1656–1659; d) R. D. Luggar, M. J. Farquharson, J. A. Horrocks, R. J. Lacey, *X-Ray Spectrometry.* **1998**, *27*, 87–94.

[11] a) M. S. Meaney, V. L. McGuffin, *Anal. Chim. Acta* **2008**, *610*, 57–67; b) M. S. Meaney, V. L. McGuffin, *Anal. Bioanal. Chem.* **2008**, *391*, 2557–2576.

[12] a) T. L. Andrew, T. M. Swager, *J. Am. Chem. Soc.* **2007**, *129*, 7254–7255; b) M. E. Germain, M. J. Knapp, *Chem. Soc. Rev.* **2009**, *38*, 2543–2555; c) M. E. Germain, T. R. Vargo, P. G. Khalifah, M. J. Knapp, *Inorg. Chem.* **2007**, *46*, 4422–4429; d) M. E. Germain, M. J. Knapp, *J. Am. Chem. Soc.* **2008**, *130*, 5422–5423; e) M. E. Germain, T. R. Vargo, B. McClure, J. J. Rack, P. G. Van Patten, M. Odoi, M. J. Knapp, *Inorg. Chem.* **2008**, *47*, 6203–6211; f) A. D. Hughes, I. C. Glenn, A. D. Patrick, A. Ellington, E. V. Anslyn, *Chem. Eur. J.* **2008**, *14*, 1822–1827.

[13] a) S. Ghosh, P. S. Mukherjee, *Organometallics* **2008**, *27*, 316–319; b) S. Shanmugaraju, H. Jadhav, Y. P. Patil, P. S. Mukherjee, *Inorg. Chem.* **2012**, *51*, 13072–13074; c) S. Shanmugaraju, S. A. Joshi, P. S. Mukherjee, *Inorg. Chem.* **2011**, *50*, 11736–11745; d) A. K. Bar, S. Shanmugaraju, K. W. Chi, P. S. Mukherjee, *Dalton Trans.* **2011**, *40*, 2257–2267.

[14] a) B. Gole, S. Shanmugaraju, A. K. Bar, P. S. Mukherjee, *Chem. Commun.* **2011**, *47*, 10046–10048; b) S. Shanmugaraju, H. Jadhav, R. Karthik, P. S. Mukherjee, *RSC Adv.* **2013**, *3*, 4940–4950.

[15] a) M. E. Kose, B. A. Harruff, Y. Lin, L. M. Veca, F. S. Lu, Y. P. Sun, *J. Phys. Chem. B* **2006**, *110*, 14032–14034; b) E. S. Snow, F. K. Perkins, E. J. Houser, S. C. Badescu, T. L. Reinecke, *Science* **2005**, *307*, 1942–1945.

[16] a) J. S. Yang, T. M. Swager, *J. Am. Chem. Soc.* **1998**, *120*, 11864–11873; b) D. T. McQuade, A. E. Pullen, T. M. Swager, *Chem. Rev.* **2000**, *100*, 2537–2574; c) S. W. Thomas, G. D. Joly, T. M. Swager, *Chem. Rev.* **2007**, *107*, 1339–1386; d) H. Sohn, R. M. Calhoun, M. J. Sailor, W. C. Trogler, *Angew. Chem.* **2001**, *113*, 2162–2163; *Angew. Chem. Int. Ed.* **2001**, *40*, 2104–2105; e) H. Sohn, M. J. Sailor, D. Magde, W. C. Trogler, *J. Am. Chem. Soc.* **2003**, *125*, 3821–3830; f) H. Cavaye, P. E. Shaw, X. Wang, P. L. Burn, S.-C. Lo, P. Meredith, *Macromolecules* **2010**, *43*, 10253–10261; g) K. K. Kartha, S. S. Babu, S. Srinivasan, A. Ajayaghosh, *J. Am. Chem. Soc.* **2012**, *134*, 4834–4841.

[17] a) H. Cavaye, H. Barcena, P. E. Shaw, P. L. Burn, S.-C. Lo, P. Meredith, *Proc. SPIE.* **2009**, *7418*, 741803; b) H. Cavaye, A. R. G. Smith, M. James, A. Nelson, P. L. Burn, I. R. Gentle, S. C. Lo, P. Meredith, *Langmuir* **2009**, *25*, 12800–12805; c) D. A. Olley, E. J. Wren, G. Vamvounis, M. J. Fernee, X. Wang, P. L. Burn, P. Meredith, P. E. Shaw, *Chem. Mater.* **2011**, *23*, 789–794; d) S. Richardson, H. S. Barcena, G. A. Turnbull, P. L. Burn, I. D. W. Samuel, *Appl. Phys. Lett.* **2009**, *95*, 063305; e) A. Narayanan, O. P. Varnavski, T. M. Swager, T. Goodson III, *J. Phys. Chem. C* **2008**, *112*, 881–884; f) M. Guo, O. Varnavski, A. Narayanan, O. Mongin, J. P. Majoral, M. Blanchard-Desce, T. Goodson III, *J. Phys. Chem. A* **2009**, *113*, 4763–4771.

[18] a) A. J. Lan, K. H. Li, H. H. Wu, D. H. Olson, T. J. Emge, W. Ki, M. C. Hong, J. Li, *Angew. Chem.* **2009**, *121*, 2370–2374; *Angew. Chem. Int. Ed.* **2009**, *48*, 2334–2338; b) C. Zhang, Y. Che, Z. Zhang, X. Yang, L. Zang, *Chem. Commun.* **2011**, *47*, 2336–2338; c) Z. Zhang, S. Xiang, X. Rao, Q. Zheng, F. R. Fronczek, G. Qian, B. Chen, *Chem. Commun.* **2010**, *46*, 7205–7207; d) S. Pramanik, C. Zheng, X. Zhang, T. J. Emge, J. Li, *J. Am. Chem. Soc.* **2011**, *133*, 4153–4155; e) B. Gole, A. K. Bar, P. S. Mukherjee, *Chem. Commun.* **2011**, *47*, 12137–12139; f) J. H. Wang, M. Li, D. Li, *Chem. Sci.* **2013**, *4*, 1793–1801; g) S. S. Nagarkar, B. Joarder, A. K. Chaudhari, S. Mukherjee, S. K. Ghosh, *Angew. Chem.* **2013**, *125*, 2953–2957; *Angew. Chem. Int. Ed.* **2013**, *52*, 2881–2885; h) G.-l. Liu, Y.-j. Qin, L. Jing, G.-y. Wei, H. Li, *Chem. Commun.* **2013**, *49*, 1699–1701.

[19] a) O. M. Yaghi, M. O'Keeffe, N. W. Ockwig, H. K. Chae, M. Eddaoudi, J. Kim, *Nature* **2003**, *423*, 705–714; b) S. Kitagawa, R. Kitaura, S. Noro, *Angew. Chem.* **2004**, *116*, 2388–2430; *Angew. Chem. Int. Ed.* **2004**, *43*, 2334–2375; c) M. W. Bennett, M. P. Shores, M. G. Beauvais, J. R. Long, *J. Am. Chem. Soc.* **2000**, *122*, 6664–6668; d) M. O'Keeffe, O. M. Yaghi, *Chem. Rev.* **2012**, *112*, 675–702; e) N. Stock, S. Biswas, *Chem. Rev.* **2012**, *112*, 933–969.

[20] a) M. P. Suh, H. J. Park, T. K. Prasad, D. W. Lim, *Chem. Rev.* **2012**, *112*, 782–835; b) K. Sumida, D. L. Rogow, J. A. Mason, T. M. McDonald, E. D. Bloch, Z. R. Herm, T. H. Bae, J. R. Long, *Chem. Rev.* **2012**, *112*, 724–781; c) M. Eddaoudi, J. Kim, N. Rosi, D. Vodak, J. Wachter, M. O'Keeffe, O. M. Yaghi, *Science* **2002**, *295*, 469–472; d) S. S. Y. Chui, S. M. F. Lo, J. P. H. Charmant, A. G. Orpen, I. D. Williams, *Science* **1999**, *283*, 1148–1150; e) A. M. Shultz, O. K. Farha, J. T. Hupp, S. T. Nguyen, *J. Am. Chem. Soc.* **2009**, *131*, 4204–4205; f) L. J. Murray, M. Dincă, J. Yano, S. Chavan, S. Bordiga, C. M. Brown, J. R. Long, *J. Am. Chem. Soc.* **2010**, *132*, 7856–7857; g) A. O. Yazaydın, R. Q. Snurr, T. H. Park, K. Koh, J. Liu, M. D. LeVan, A. I. Benin, P. Jakubczak, M. Lanuza, D. B. Galloway, J. L. Low, R. R. Willis, *J. Am. Chem. Soc.* **2009**, *131*, 18198–18199.

[21] a) J. R. Li, R. J. Kuppler, H. C. Zhou, *Chem. Soc. Rev.* **2009**, *38*, 1477–1504; b) J. R. Li, J. Sculley, H. C. Zhou, *Chem. Rev.* **2012**, *112*, 869–932; c) H. S. Choi, M. P. Suh, *Angew. Chem.* **2009**, *121*, 6997–7001; *Angew. Chem. Int. Ed.* **2009**, *48*, 6865–6869; d) J. An, S. J. Geib, N. L. Rosi, *J. Am. Chem. Soc.* **2010**, *132*, 38–39; e) Y. E. Cheon, J. Park, M. P. Suh, *Chem. Commun.* **2009**, 5436–5438; f) C. Y. Lee, Y.-S. Bae, N. C. Jeong, O. K. Farha, A. A. Sarjeant, C. L. Stern, P. Nickias, R. Q. Snurr, J. T. Hupp, S. T. Nguyen, *J. Am. Chem. Soc.* **2011**, *133*, 5228–5231; g) R. Matsuda, R. Kitaura, S. Kitagawa, Y. Kubota, R. V. Belosludov, T. C. Kobayashi, H. Sakamoto, T. Chiba, M. Takata, Y. Kawazoe, Y. Mita, *Nature* **2005**, *436*, 238–241; h) J. P. Zhang, X. M. Chen, *J. Am. Chem. Soc.* **2008**, *130*, 6010–6017.

[22] a) J. An, S. J. Geib, N. L. Rosi, *J. Am. Chem. Soc.* **2009**, *131*, 8376–8377; b) P. Horcajada, C. Serre, M. Vallet-Regi, M. Sebban, F. Taulelle, G. Ferey, *Angew. Chem.* **2006**, *118*, 6120–6124; *Angew. Chem. Int. Ed.* **2006**, *45*, 5974–5978; c) P. Horcajada, T. Chalati, C. Serre, B. Gillet, C. Sebrie, T. Baati, J. F. Eubank, D. Heurtaux, P. Clayette, C. Kreuz, J. S. Chang, Y. K. Hwang, V. Marsaud, P. N. Bories, L. Cynober, S. Gil, G. Férey, P. Couvreur, R. Gref, *Nat. Mater.* **2010**, *9*, 172–178.

[23] a) K. M. L. Taylor, W. J. Rieter, W. Lin, *J. Am. Chem. Soc.* **2008**, *130*, 14358–14359; b) J. Della Rocca, D. M. Liu, W. B. Lin, *Acc. Chem. Res.* **2011**, *44*, 957–968.

[24] a) L. Q. Ma, C. Abney, W. B. Lin, *Chem. Soc. Rev.* **2009**, *38*, 1248–1256; b) A. Corma, H. Garcia, F. X. L. Xamena, *Chem. Rev.* **2010**, *110*, 4606–4655; c) M. Yoon, R. Srirambalaji, K. Kim, *Chem. Rev.* **2012**, *112*, 1196–1231; d) D. Farrusseng, S. Aguado, C. Pinel, *Angew. Chem.* **2009**, *121*, 7638–7649; *Angew. Chem. Int. Ed.* **2009**, *48*, 7502–7513; e) Y. Liu, W. M. Xuan, Y. Cui, *Adv. Mater.* **2010**, *22*, 4112–4135.

[25] a) B. L. Chen, S. C. Xiang, G. D. Qian, *Acc. Chem. Res.* **2010**, *43*, 1115–1124; b) L. E. Kreno, K. Leong, O. K. Farha, M. Allendorf, R. P. V. Duyne, J. T. Hupp, *Chem. Rev.* **2012**, *112*, 1105–1125; c) Z. Z. Lu, R. Zhang, Y.-Z. Li, Z. J. Guo, H. G. Zheng, *J. Am. Chem. Soc.* **2011**, *133*, 4172–4174; d) Y. Takashima, V. M. Martinez, S. Furukawa, M. Kondo, S. Shimomura, H. Uehara, M. Nakahama, K. Sugimoto, S. Kitagawa, *Nat. Commun.* **2011**, *2*, 168; e) B. Gole, A. K. Bar, A. Mallick, R. Banerjee, P. S. Mukherjee, *Chem. Commun.* **2013**, *49*, 7439–7441; <lit f>R. K. Das, A. Aijaz, M. K. Sharma, P. Lama, P. K. Bharadwaj, *Chem. Eur. J.* **2012**, *18*, 6866–6872.

[26] a) Y. Cui, Y. Yue, G. Qian, B. Chen, *Chem. Rev.* **2012**, *112*, 1126–1162; b) J. An, C. M. Shade, D. A. Chengelis-Czegan, S. P. Petoud, N. L. Rosi, *J. Am.*

Chem. Soc. **2011**, *133*, 1220–1223; c) K. Jayaramulu, P. Kanoo, S. J. George, T. K. Maji, *Chem. Commun.* **2010**, *46*, 7906–7908.

[27] a) A. Saha, S. Ramakrishnan, *Macromolecules* **2009**, *42*, 4956–4959; b) T. B. Faust, V. Bellini, A. Candini, S. Carretta, G. Lorusso, D. R. Allan, L. Carthy, D. Collison, R. J. Docherty, J. Kenyon, J. Machin, E. J. L. McInnes, C. A. Muryn, H. Nowell, R. G. Pritchard, S. J. Teat, G. A. Timco, F. Tuna, G. F. S. Whitehead, W. Wernsdorfer, M. Affronte, R. E. P. Winpenny, *Chem. Eur. J.* **2011**, *17*, 14020–14030.

[28] SMART/SAINT, Bruker AXS, Inc., Madison, WI, **2004**.

[29] G. M. Sheldrick, SADABS, University of Göttingen, Göttingen, Germany, **1999**.

[30] G. M. Sheldrick, SHELX-97, University of Göttingen, Göttingen, Germany, **1998**.

[31] a) L. J. Farrugia, *J. Appl. Crystallogr.* **1999**, *32*, 837; b) L. J. Farrugia, WinGX, version 1.65.04, Department of Chemistry, University of Glasgow, Glasgow, Scotland, **2003**.

[32] B. Delley, *J. Chem. Phys.* **1990**, *92*, 508–517.

[33] B. Delley, *J. Chem. Phys.* **2000**, *113*, 7756–7764.

[34] Material Studio DMOL3, Version 6.0. Accelrys, Inc., San Diego, USA.

Received: June 26, 2013
Revised: November 15, 2013